Horizon 2020 Programme

GENIORS

Research and Innovation Action (RIA)

This project has received funding from the European Union's Horizon 2020 research and innovation programme under grant agreement No 755171.

Start date : 2017-06-01 Duration : 48 Months
http://geniors.eu/

GENIORS

Impact of the precursor "history" (nature, structural, microstructural and morphological parameters) during the conversion and sintering to actinide based dioxide materials

Authors : Mr. Nicolas DACHEUX (CEA), Nicolas Clavier (CNRS), Jérémie Manaud (UM), Morgan Zunino (CNRS), Malvina Massonnet (CEA), Victor Trillaud (CEA), Adel Mesbah (CNRS), Renaud Podor (CNRS), Nicolas Dacheux (UM)

GENIORS - Contract Number: 755171

Project officer: Roger Garbil

Document title	Impact of the precursor "history" (nature, structural, microstructural and morphological parameters) during the conversion and sintering to actinide based dioxide materials
Author(s)	Mr. Nicolas DACHEUX, Nicolas Clavier (CNRS), Jérémie Manaud (UM), Morgan Zunino (CNRS), Malvina Massonnet (CEA), Victor Trillaud (CEA), Adel Mesbah (CNRS), Renaud Podor (CNRS), Nicolas Dacheux (UM)
Number of pages	59
Document type	Deliverable
Work Package	WP4
Document number	D4.4
Issued by	CEA
Date of completion	2021-03-07 12:33:42
Dissemination level	Public

Summary

Within the development of new generations of reactors, wet chemistry routes are studied for the fabrication of mixed oxide fuels such as (U,Pu)O2 MOx, notably to improve the cations distribution homogeneity. In this framework, our work aimed at directly synthesizing uranium-based oxide samples from solution using hydrothermal conditions, and evaluate their sintering ability. Samples were first prepared through the hydrothermal conversion of oxalate precursors between 180°C and 250°C. These conditions allowed the systematic formation of UO2+x, nH2O, even if HERFD-XANES analyses evidenced variations in the O/U ratio. Moreover, hydrothermal treatment at 250°C led to very low amounts of residual water and carbon, comparable to those obtained after thermal conversion of oxalates at 1000°C. Modifying the pH was also found to strongly affect the morphology of the final powders. Control on the final morphology was further enhanced by changing the precipitating agent used before hydrothermal treatment. Hydrothermal conversion of amorphous U(IV) aspartate led to precipitate monodisperse spherical particles, with an accurately size control in the 400 nm ? 2.5 µm range. Once again, XRD analysis attested the formation of UO2+x.nH2O samples, while TGA experiments revealed the presence of residual organics and water. Nevertheless, additional heat treatments performed up to 600°C led to produce anhydrous and carbon-free dense particles without altering their initial morphology. It also enabled to control the final stoichiometry of the particles from UO2+x to U3O8 depending on the atmosphere used. Hydrothermal conversion of carboxylate precursors then appeared as an easy and efficient way to yield uranium oxide samples in solution. The absence of impurities as well as the possibility to monitor the samples morphology also allow the direct sintering of the powders prepared. A preliminary study dedicated to sintering of the powders prepared was then undertaken and revealed their good densification ability. The sintering map of 3 different uranium oxides presenting different morphologies was established, and paves the way to the control of the final pellet?s microstructure. The study of the densification revealed that after a 4-hours heat treatment at 1500°C, all the powders exhibited relative densities above 90%TD. In the case of single crystals and microspheres, densities greater than or equal to 96% were also obtained at 1700°C. In contrast, a sintering time o...

Approval

Date	By
2021-03-07 12:37:10	Mr. Nicolas DACHEUX (CEA)
2021-03-08 08:30:13	Mr. Andreas GEIST (KIT)
2021-03-10 14:33:55	Mr. Stéphane BOURG (CEA)

GENIORS

GEN IV integrated oxide fuels recycling strategies

DELIVRABLE D4.4. Impact of the precursor “history” (nature, structural, microstructural and morphological parameters) during the conversion and sintering to actinide based dioxide materials

Author(s): Nicolas Clavier, Jérémie Manaud, Morgan Zunino, Malvina Massonnet, Victor Trillaud, Adel Mesbah, Renaud Podor, Nicolas Dacheux

Version: 2 issued on 07/03/2021

This project has received funding from the EURATOM research and training programme 2017-2021 under grant agreement No 755171

CONTENT

This project has received funding from the EURATOM research and training programme 2017-2021 under grant agreement No 755171

EXECUTIVE SUMMARY

The deliverable D4.4. *Impact of the precursor "history" (nature, structural, microstructural and morphological parameters) during the conversion and sintering to actinide-based dioxide materials*) deals with the conversion of cations in solution to final sintered pellets by using various uranium lanthanide bearing precursors (Task 4.2.). This task is strongly connected to Task 4.1. in which the optimization of the dissolution of various uranium bearing oxide solid solutions has been carried out in conditions representative for the reprocessing step prior the recycling of actinides (see deliverable D4.1. *Understanding the evolution of an interface during dissolution of actinide oxide materials by macro-/microscopic approaches combination*).

INTRODUCTION

Already commonly used in light water nuclear reactors worldwide, uranium (UO_2) and uranium-plutonium dioxides ($(U,Pu)O_2$, also known as MOx) are also envisaged as reference fuels for future generations of fast neutron reactors, such as SFR (Sodium-cooled Fast Reactor) [1, 2]. Beyond the opportunities offered by such reactors, the transition from thermal to fast neutron spectra will allow to rethink plutonium management. Particularly, multi-recycling MOx is envisaged to close the fuel cycle [3]. In order to face these technological challenges, the fabrication of the fuel ceramic has to be optimized. Especially, homogeneous mixed oxides must be produced to prevent the existence of Pu-enriched hot spots during in-core lifetime, that can also become refractory towards dissolution during the reprocessing step [4]. Numerous studies then considered wet chemistry methods to precipitate homogeneous precursors (i.e. solid solutions) from ions in solution [5].

Among the various complexing agents investigated to co-precipitate cations mixtures, oxalates dragged important attention, mainly due to their rich crystal chemistry which allows the incorporation of actinides with different redox states (e.g. U(IV) and Pu(III)) within an unique structural lattice [6]. The final oxide is further obtained after a heat treatment at high temperature (typically from 700 to 1000°C) under controlled atmosphere, called thermal conversion [7, 8]. Although very convenient, and already used industrially to recover plutonium after UO_2 spent fuel reprocessing, oxalic conversion still presents some limitations. First, the precipitation of An(IV) oxalates is generally associated to a square-shaped platelets habit that is further retained within the oxide powder [9]. This morphological feature can limit the powder flowability when shaping pellets for ceramic fabrication, and then induce some mechanical defects after sintering. Also, oxides powders coming from oxalate precursors generally incorporate residual traces of carbon, typically from around 100 ppm when calcined under air [10] up to several thousands of ppm for thermal conversion performed under inert or reducing atmospheres [9], which have been associated to de-densification processes [11, 12].

In order to avoid these potential issues and to get rid of the thermal conversion step, we investigated in the frame of the GENIORS project the use of hydrothermal conditions to directly achieve actinide oxide precipitation from solution. By these means, the precipitation of the cations is ensured by the use of an organic complexing agent, which is further degraded *in situ* by the combined action of temperature and pressure. Simultaneously, actinides are hydrolyzed

This project has received funding from the EURATOM research and training programme 2017-2021 under grant agreement No 755171

to form hydroxo- or oxohydroxo- species that finally age into oxides [13]. On this basis, the first part of this deliverable will be focused on the hydrothermal conversion of U(IV)-based oxalate then aspartate precursors into uranium oxides, while the precipitation of uranium (IV) hydroxides will be presented as a reference way for the preparation of highly sinterable powders. Multi-parametric studies were undertaken in order to unravel the effects of temperature, pH, time, … on the precipitation and get advanced insights on the hydrothermal conversion mechanism. For all the samples prepared, a complete characterization was achieved at the structural, morphological and chemical levels.

The precipitation of U(IV)-based oxides from ions in solution also paves the way to the direct sintering of the raw samples obtained after hydrothermal treatment of the precursors, which would offer a compact process going from ions in solution to fuel pellet in a few steps. The second part of this report will then be devoted to the sintering of an exhaustive set of UO_{2+x} samples obtained in various conditions of hydrothermal treatment. Three representative powders were first selected to build sintering map and link the conditions of synthesis with the final microstructure of the ceramics. Preliminary results regarding the grain growth mechanisms and the activation energy related to the sintering of these powders are also reported herein. Finally, the synthesis of size-controlled UOx microspheres through the hydrothermal conversion of uranium (IV) aspartate also allowed us to go deeper into the sintering mechanism by using in situ High-Temperature Environmental Scanning Electron Microscopy (HT-ESEM) observations.

Brought together, these studies aim to demonstrate that hydrothermal conversion of carboxylate precursors can be considered as a promising route for the synthesis of actinide oxides, which can subsequently be sintered without preliminary treatment. More importantly, controlling the precursor “history” (nature, structural, microstructural and morphological parameters) and conversion conditions could allow to control more accurately the final microstructure of the pellets obtained after sintering.

This project has received funding from the EURATOM research and training programme 2017-2021 under grant agreement No 755171

MAIN RESULTS

SYNTHESIS OF URANIUM-BASED OXIDES WITH CONTROLLED MORPHOLOGY USING HYDROTHERMAL CONDITIONS

PREPARATION OF HIGHLY HOMOGENOUS $(U,Ce)O_{2\pm\delta}$ AS REFERENCE MATERIALS

As a final aim of this study is to prepare homogeneous oxide materials with a high densification capability from hydrothermal conversion of carboxylate precursors, $(U,Ce)O_{2\pm\delta}$ were first produced by hydroxide precipitate to get a reference material. This process was already proved to yield highly homogeneous distribution of the cations within the sample, coupled to a nanometric size of the powder enhancing the sinterability. These samples were also used for the dissolution studies reported in the Deliverable 4.1. *Understanding the evolution of an interface during dissolution of actinide oxide materials by macro-/microscopic approaches combination*.

Synthesis

The preparation of the hydroxide precursors started from a mixture of uranium (IV) chloride and of cerium (IV) sulphate (≈ 0.05 M) solutions, in the desired stoichiometric ratio x = Ce/(U + Ce). Such mixture was then poured into a large excess of ammonium hydroxide (400%) at room temperature, leading to the instantaneous formation of a precipitate. This latter was further aged in solution for one hour under magnetic stirring. The powders precipitated were then separated from the supernatant by centrifugation at 4500 rpm. The freshly prepared precipitates were finally washed several times with deionized water then once with ethanol in order to eliminate all remaining traces of ammonium hydroxide. For all the chemical compositions investigated, the supernatants collected after the precipitation step were analysed by Inductively-Coupled Plasma Atomic Emission Spectroscopy (ICP-AES, Spectro Arcos) to determine the precipitation yield of the cations. The precipitation of both cations appeared systematically to be quantitative, with yield values ≥ 99 %.

Characterization of the precursors

The powdered samples obtained after the synthesis procedure described above and further de-agglomeration step were then first investigated by the means of Powder X-Ray Diffraction (PXRD). For all the chemical compositions considered, the PXRD patterns collected (**Figure 1**) exhibited wide XRD lines (large FWHM) that fitted with the cubic fluorite-type structure (Fm-3m space group), characteristic of both CeO_2 [14] and actinide dioxides [15]. From these data, the precipitation of a partly amorphous hydrated oxide was found to be the most credible hypothesis, albeit the formation of such compound could also occur through the ageing of an initial hydroxide form, for example during the drying procedure, considering the following reaction:

$$U_{1-x}Ce_x(OH)_4 \rightarrow U_{1-x}Ce_xO_2.\ nH_2O + (2-n)\ H_2O \qquad \textbf{(1.)}$$

This project has received funding from the EURATOM research and training programme 2017-2021 under grant agreement No 755171

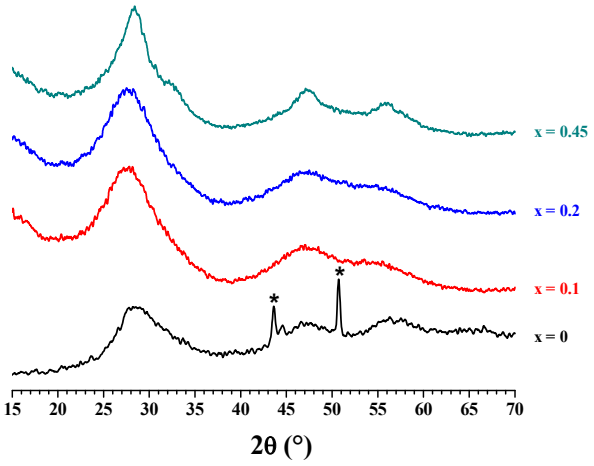

Figure 1. XRD patterns of the $U_{1-x}Ce_xO_2$. n H_2O (x = 0, 0.1, 0.2, 0.45) precursors. The main XRD lines of sample holder are indicated by a star (*).

The large width of the peaks recorded revealed that the samples prepared were poorly crystallized and/or nanosized. This feature was confirmed by the Rietveld refinement of the PXRD which allowed the determination of the length of coherent domains (i.e. average crystallite size). Only small variations of the average crystallite size were observed depending on the chemical composition considered, with values ranging from 1.0 nm for x = 0 to 1.5 nm for x = 0.45. In these conditions, the incorporation of cerium in the structure could appear to slightly increase the crystal growth during the precipitation process. Such modification could be linked to the presence of small amounts of trivalent cerium in the solid that could increase the diffusion of cations [16, 17].

The morphology of the hydroxide precursors was then investigated by the means of scanning (SEM) and transmission (TEM) electron microscopies. Whatever the chemical composition considered, the SEM micrographs recorded (**Figure 2**) systematically revealed a similar aspect. The powdered samples were found to be composed of very small particles with a size in the nanometer range. In spite of the drying step performed under vacuum, some large aggregates (ranging from 10 to 20 µm) still remained. They could have resulted from the preparation of the sample before the observation (deposition on a carbon stick) and/or from the high vacuum used in the SEM chamber. Still, despite of the partial aggregation of the nanosized crystallites, specific surface area measurements through the BET method confirmed the very high reactivity of the powders prepared. Indeed, the values obtained all ranged between 130 and 150 $m^2.g^{-1}$, again independently from the cerium incorporation rate considered.

Finally, EDS analyses were also coupled to SEM observations, which allowed the evaluation of the cationic homogeneity of the powdered samples at the micrometer scale. Whatever the chemical composition considered, the average chemical composition of the samples was found to be in a very good agreement with that calculated (**Table 1**). The precipitation of the hydroxide precursors was thus quantitative. Also, the distribution of the analyses results around the average value was narrowed, thus evidencing the very good homogeneity of the samples prepared at the micrometer scale. As a matter of comparison, the distribution of the Ce/(U+Ce) mole ratio was found to be significantly narrowed compared to the results reported for $(Th,U)O_2$ mixed oxides prepared from oxalate precursors, even when using hydrothermal conditions [18].

This project has received funding from the EURATOM research and training programme 2017-2021 under grant agreement No 755171

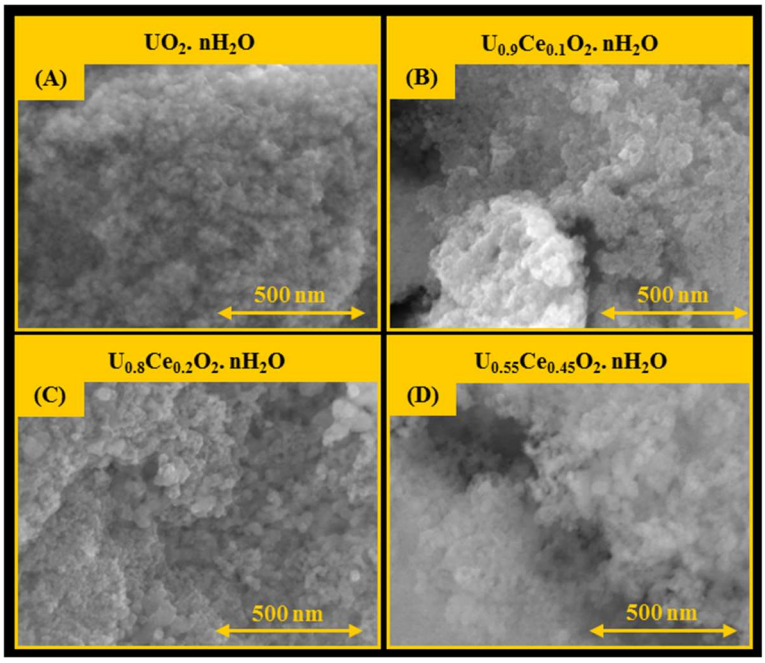

Figure 2. Scanning electron micrographs of powdered $U_{1-x}Ce_xO_2 . nH_2O$ with x = 0 (A), x = 0.1 (B), x = 0.2 (C) and x = 0.45 (D).

Table 1. Results of statistical EDS analyses obtained for $U_{1-x}Ce_xO_2 . nH_2O$ samples.

$x_{calc.}$	U (wt.%)	U (at.%)	Ce (wt.%)	Ce (at. %)	$x_{exp.}$
0.1	72.0 ± 0.3	30.0 ± 0.1	5.0 ± 0.3	3.3 ± 0.2	0.10 ± 0.01
0.2	63.9 ± 0.3	26.7 ± 0.1	9.7 ± 0.3	6.7 ± 0.2	0.20 ± 0.01
0.45	44.5 ± 0.3	18.3 ± 0.1	21.1 ± 0.3	15.0 ± 0.2	0.45 ± 0.01

Conclusion

The hydrothermal conversion of (U,Ce) mixed oxalates then appears to be a complex case, mainly because of the redox chemistry of cerium and its possible interplay with that of uranium. Nevertheless, additional operating parameters that were not investigating during this work, such as the concentration of cations in the starting solution of the solid/liquid ratio in the hydrothermal reactor, remain potential leverages to allow the quantitative precipitation of uranium and cerium within homogeneous oxide phases.

HYDROTHERMAL CONVERSION OF U-BASED OXALATES

A multi-parametric study focused on the hydrothermal conversion of uranium (IV) oxalate $U(C_2O_4)_2.nH_2O$ into uranium bearing oxides was undertaken in order to unravel the effects of temperature, pH and holding time. All the samples were prepared from the precipitation of uranium (IV) oxalate and its subsequent conversion into oxides under mild hydrothermal conditions. The initial precipitation was obtained by mixing about 0.5 mmol of uranium (IV) chloride solution with a 50 mol.% excess of oxalic acid (0.5M). Mixture of the reagents rapidly led to the formation of a greenish precipitate. Afterwards, both the solid phase and the supernatant were transferred in a Teflon-lined autoclave (Parr). Whatever the operating conditions considered, the volume of the solution was adjusted to 15 mL by adding 0.5 M HCl

This project has received funding from the EURATOM research and training programme 2017-2021 under grant agreement No 755171

in order to avoid any bias due to autogenous pressure during the hydrothermal treatment. The pH of the resulting solution was generally below 0.5 and was further adjusted by addition of diluted NH_4OH and hydrochloric acid solution.

The reactor was finally sealed then heated between 130 to 250°C for 1 to 48 hours. As a matter of example, the pressure was close to 80 bars at 250°C [19]. The autoclave was cooled down naturally before collection of the final precipitate. This latter was separated by centrifugation at 14000 rpm, washed twice with deionized water and twice with ethanol then finally dried overnight at 90°C in an oven.

Effect of temperature

The effect of the hydrothermal treatment temperature on the physico-chemical properties of the powders prepared was first investigated between 130 and 250°C. With this aim, the duration of the hydrothermal treatment was arbitrarily set to 24 hours whereas the pH of the reacting media remained uncontrolled and was then systematically found to be strongly acidic (*i.e.* pH < 1). Additionally, a sample that did not undergo any hydrothermal treatment was prepared and considered as a reference obtained at room temperature.

The samples obtained after hydrothermal treatment between 130 and 250°C were first characterized by PXRD (**Figure 3**). The reference sample prepared without any hydrothermal treatment confirmed the precipitation of $U(C_2O_4)_2.2H_2O$ from the mixture of U(IV) chloride solution and oxalic acid. Indeed, the PXRD diagram collected presented all the XRD lines characteristic of the monoclinic structure (C2/c space group) reported by Clavier *et al.* [20] (see the stick pattern in **Figure 3a**). $U(C_2O_4)_2.2H_2O$ was further maintained when applying hydrothermal treatments up to 160°C. A slight modification of the PXRD diagram was noted at 170°C, likely due to the partial dehydration of the oxalate.

In contrast, all the PXRD patterns recorded for samples prepared for temperatures higher than 180°C were found to present all the characteristic XRD lines of UO_{2+x} (fluorite-type structure) [21]. The hydrothermal conversion of the oxalate species then occurred on a very narrow temperature range. This observation was backed up by the determination of the uranium (IV) precipitation yield. Indeed, for the lowest temperatures investigated (i.e. up to 130°C), this precipitation yield remained close to the value determined for the oxalate obtained at RT and was considered as almost quantitative, in good agreement with the abundant literature dedicated to uranium oxalates [22, 23]. The synthesis yield was then found to drastically decrease down to only 15% at around 170°C, which marked the transition from oxalate to oxide. This temperature was in good agreement with the literature, since Crossey reported the decomposition of aqueous oxalate species in the 180-230°C range [24]. Oxalates were found to evolve to formic acid species following a first-order kinetic law, the reaction rate being increased for low pH values and high temperatures.

For higher temperatures, the synthesis yield increased progressively between 180 and 200°C then stabilized up to 250°C to reach about 70%. U(IV) was then partly precipitated in these conditions, which could be explained by the very low pH of the solution (i.e. pH < 1). Indeed, after the initial decomposition of the oxalate moieties, the formation of the oxide was likely to occur through the formation of hydroxides, which further rapidly aged to form $UO_{2+x}.nH_2O$. The formation of $U(OH)_4$ (i.e. total hydrolysis of U^{4+}) was then incomplete in our experimental conditions, which tended to lower the precipitation yield.

This project has received funding from the EURATOM research and training programme 2017-2021 under grant agreement No 755171

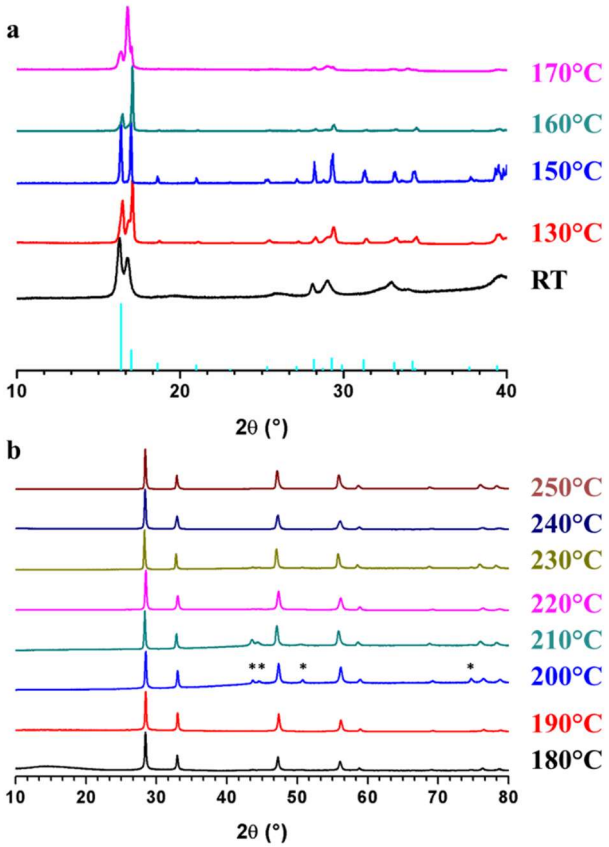

Figure 3. XRD patterns obtained after hydrothermal treatment of $U(C_2O_4)_2.nH_2O$ at various temperatures during 24h : a) RT - 170°C, b) 180°C - 250°C. Stick pattern in figure a) is taken from PDF data file #01-078-7197. * : XRD lines assigned to the sample holder.

In order to complete the structural characterization of the uranium oxide samples, Rietveld refinements of the PXRD patterns were performed with the aim to extract the unit cell volumes and average crystallite sizes (**Figure 4**). As a preliminary approach, only one fluorite-type structure, corresponding to a single UO_{2+x} phase, was considered in the fitting procedure. Therefore, the derived lattice parameter was merely a qualitative indicator of the oxide stoichiometry, i.e. of uranium oxidation state.

Whatever the temperature considered in the 180-250°C range, the unit cell volume was systematically found to be lower than the reference value recently reported by Leinders *et al.* for $UO_{2.00}$ [25] (163.781 Å^3). This clearly indicated the formation of hyper-stoichiometric oxides, as the unit cell volume of UO_{2+x} was reported for long to vary from 163.5-163.8 Å^3 for $UO_{2.00}$ [26, 27] to around 161.0 Å^3 for O/U ratios close to 2.25 [28-30], which constitutes the upper limit of the fluorite-type structure ($UO_{2.25}$ being indexed in the R3c or the I-43d space group depending on the temperature considered [31]). Thus, two temperature ranges can be distinguished depending on the value of the unit cell volume.

From 180 to 210°C, all the hydrothermal treatments led to unit cell volumes below the limit value of 161.0 Å^3, which could be interpreted as a strong increase of the O/U ratio in the samples. On this basis, one must envisage that the use of hydrothermal conditions, combined with the submicrometric size of the powders (see below) might have stabilized a fluorite-derived structure towards higher values of O/M ratio. Indeed, cubic UO_{2+x} samples with x =

This project has received funding from the EURATOM research and training programme 2017-2021 under grant agreement No 755171

0.24 – 0.5 were already reported after oxidation of ultra-fine $UO_{2.00}$ in air at room temperature [32, 33]. In the 220-250°C range, the unit cell volume of the samples prepared was further found to increase, which could be seen as a decrease of the O/U ratio in hyper-stoichiometric UO_{2+x} samples, or of the U_4O_9 amount in UO_{2+x} / U_4O_9 mixtures. However, the direct correlation of the lattice parameters with an accurate x value remains difficult in such a complex multiphase system.

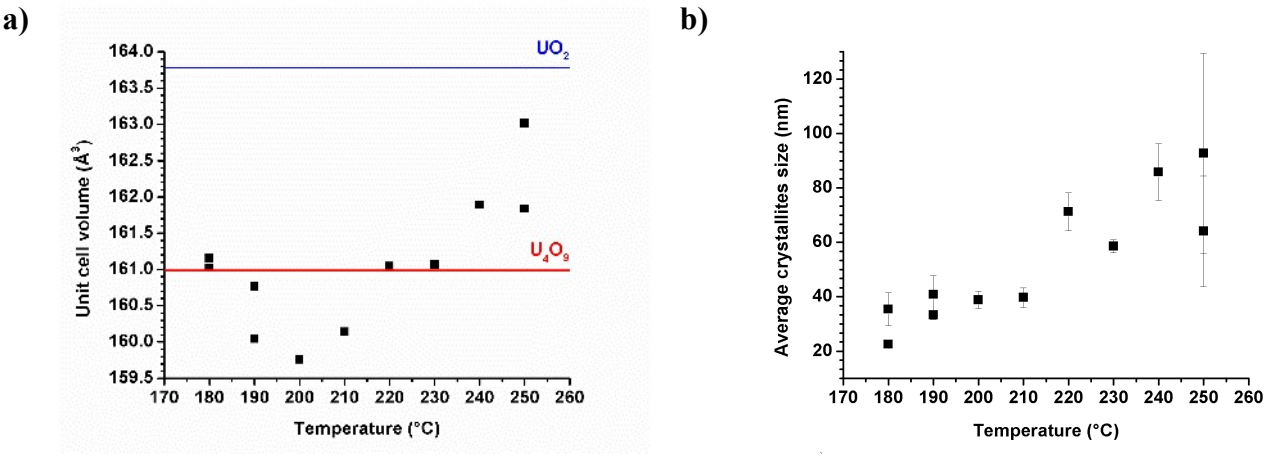

Figure 4. Variation of the unit cell volume (a) and of the average crystallites size (b) of uranium oxide (considered as a single fluorite-type structure) versus temperature of hydrothermal treatment (pH < 1, t = 24 hours). Reference values for UO_2 and U_4O_9 are taken from references [25] and [34], respectively.

Additionally, the variation of the crystallites size (**Figure 4b**) was also monitored. Even if the values obtained tend to be underestimated when considering a single fluorite-type structure instead of the real multiphase system, a general trend can be discussed. In the 180-210°C range, the crystallites size was first found to remain mostly constant and close to 30-40 nm, while growth processes were activated and led to crystallites sizes up to 90 nm for higher temperatures of hydrothermal treatment.

In order to get further insights on the O/U stoichiometry of oxides produced by hydrothermal conversion of $U(C_2O_4)_2.nH_2O$, additional HERFD-XANES experiments at the uranium M_4-edge [35] were undertaken on selected samples as well as on UO_2, U_4O_9 and U_3O_8 references (**Figure 5**).

All the spectra recorded on oxides prepared after hydrothermal conversion of uranium (IV) oxalate between 200 and 250°C presented two distinct peaks, which accounted for U(IV) / U(V) mixed valence compounds. Nevertheless, the intensity of the two peaks was systematically found to be uneven, which excluded the simple formation of U_4O_9. Also, one must note that the presence of uranyl entities was discarded in these samples due to the absence of band around 3733 eV. Moreover, significant differences were noted between the sample obtained at 200°C, and those synthesized at higher temperatures. On the one hand, the sample prepared at 200°C displayed a U(V) contribution significantly higher than the U(IV) one. A very slight band around 3732 eV was also distinguished and accounted for the presence of limited amount of U(VI) in the system. Conversely, the U(IV) was found to be predominant in samples prepared at 220°C, 240°C and 250°C.

This project has received funding from the EURATOM research and training programme 2017-2021 under grant agreement No 755171

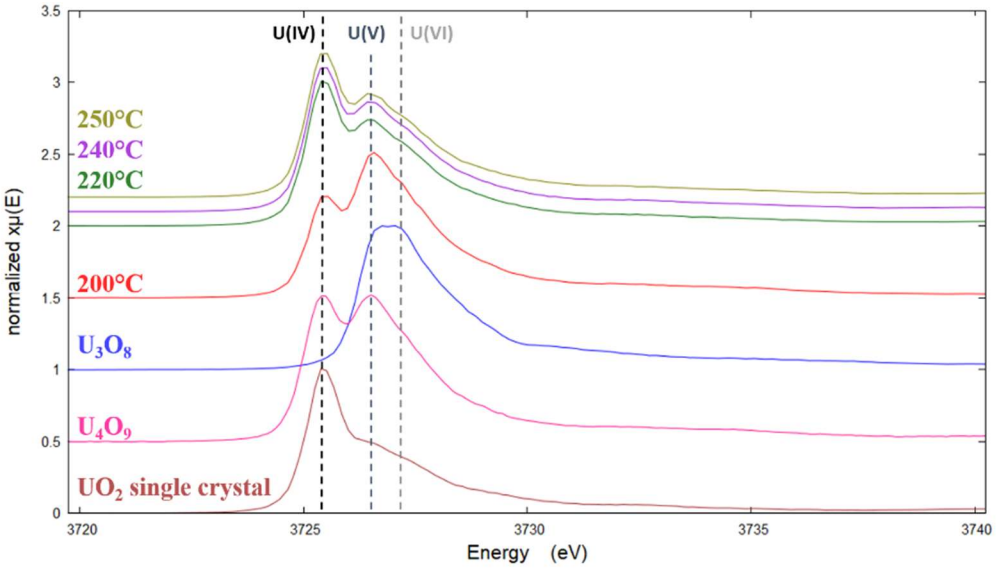

Figure 5. Normalized HERFD-XANES spectra of reference samples and of oxide samples obtained after hydrothermal treatment of $U(C_2O_4)_2.nH_2O$ at various temperatures, for 24 hours and pH < 1.

The contribution of U(IV), U(V) and U(VI) was then quantified by fitting the collected spectra as a linear combination of the three references (**Table 2**). For the sample prepared at 200°C, the spectrum was only correctly fitted by considering the three different oxidation states of uranium. On the contrary, satisfactory fit was obtained by using only a combination of UO_2 and U_4O_9 for samples synthesized between 220 and 250°C. With these results, the global O/U ratio in the samples was estimated to 2.38 ± 0.10 at 200°C and close to 2.13 ± 0.04 in the 220-250°C range. Based on the U-O phase diagram reported by Guéneau *et al.*[36], the sample prepared at 200°C should then correspond to a mixture of U_3O_7 and U_3O_8. Nevertheless, as mentioned previously, the presence of these phases was discarded from the XRD analysis. The use of hydrothermal conditions then allowed to stabilize the cubic structure of UO_{2+x} / U_4O_9 up to higher O/U ratios. On the contrary, the samples prepared at higher temperatures presented a stoichiometry corresponding to a mixture of approximately 60% $UO_{2.05}$ and 40% U_4O_9, which was in good agreement with the XRD patterns recorded.

Table 2. Uranium oxidation state distribution obtained from the linear combination fitting of HERFD-XANES spectra.

Temperature (°C)	U(IV) (%)	U(V) (%)	U(VI) (%)	O/U ratio	Average U oxidation state
200	36.0 ± 1.8	52.5 ± 1.8	11.5 ± 0.6	2.38 ± 0.10	4.8
220	76.3 ± 1.5	23.7 ± 0.5	0	2.12 ± 0.04	4.2
240	73.8 ± 1.4	26.2 ± 0.4	0	2.13 ± 0.04	4.3
250	74.9 ± 1.1	25.1 ± 0.4	0	2.13 ± 0.03	4.3

The oxide samples prepared by hydrothermal conversion of $U(C_2O_4)_2.nH_2O$ between 180 and 250°C (pH < 1; t = 24 hours) were further characterized from the morphological and chemical points of view. With this aim, SEM images were collected for selected samples (**Figure 6**).

This project has received funding from the EURATOM research and training programme 2017-2021 under grant agreement No 755171

While the oxalate samples retained their classical platelet-like habit up to 170°C, the conversion towards oxides marked a drastic modification in the powder's morphology. Indeed, as soon as 180°C, the powders were found to be formed by bipyramid-shape aggregates of about 1 µm in length. These objects were composed by smaller crystallites of about 40 nm, as evidenced from PXRD data refinement, and then possessed a hierarchical microstructure, which was frequently observed in samples obtained through hydrothermal methods [37, 38]. The use of hydrothermal conditions then allowed to get rid of the usual platelet-like morphology of An(IV) oxalates, which is expected to be poorly suitable for shaping and sintering and was always retained by using isomorphic thermal conversion.

The size and the shape of the aggregates obtained was further maintained up to 220°C, although the inner porosity substantially increased, thereby increasing the roughness. Such modification of the aggregate's microstructure was correlated to the increase of the average crystallite size with temperature, as already evidenced by PXRD measurements. In contrast, the particles obtained at 250°C were found to be smaller with sizes typically between 200 and 500 nm. This feature was likely to be linked with the kinetics of oxalate degradation which was fastened by the rise of temperature and probably favoured the nucleation of isolated particles.

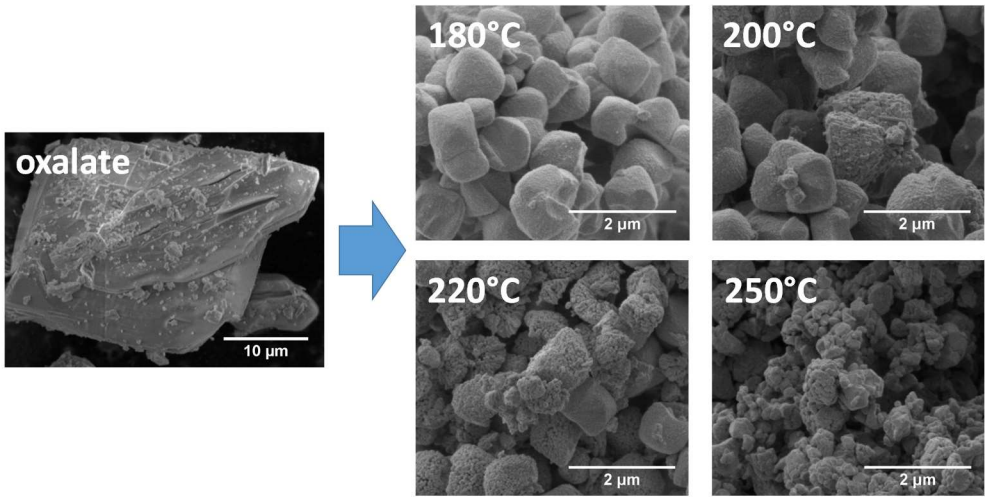

Figure 6. SEM images of uranium dioxide synthesized by hydrothermal treatment of $U(C_2O_4)_2.nH_2O$ (pH < 1, t = 24 h) at various temperatures and comparison with the starting uranium bearing oxalate precursor.

The presence of impurities coming from the hydrothermal degradation of $U(C_2O_4)_2.nH_2O$ was finally checked in the oxide samples. Indeed, previous works showed that the presence of residual carbon in the oxide powders could impact negatively the densification step[9, 11, 12]. Powders were then first characterized thanks to a carbon analyzer (**Table 3**). After heating at 180°C, the residual carbon content within the oxide powders reached 0.82 ± 0.01 wt.%. Such a huge amount might indicate that the decomposition of oxalate species was still incomplete, even if only fluorite-type oxides were detected by PXRD. Also, amorphous carbon or carbonate species could be trapped either within the oxide structure or between the crystallites forming the aggregates. Nevertheless, the carbon content was found to quickly drop down with temperature. Indeed, it was found to 0.12 ± 0.02 wt.% after heating at 200°C, which was lower than the value measured by Martinez *et al.* in UO_{2+x} oxides coming from direct conversion of $U(C_2O_4)_2.2H_2O$ under reducing atmosphere at 1000°C (i.e. 0.2 wt.%) [9]. Beyond 220°C, the value became even lower and decreased by about one order of magnitude to reach 100-200

ppm. Such amount was close to that generally reported for oxides prepared through the calcination of oxalate precursors under oxidizing atmospheres [9, 10, 39], which strongly favours the elimination of carbon through the Boudouard's equilibrium ($C/CO/CO_2$). The use of mild hydrothermal conditions then appeared as a powerful way to eliminate carbon residues from the samples and yielded highly-pure samples of uranium dioxide.

Table 3. Carbon content (expressed in wt.%) and water content (expressed in mol. per mole of oxide) obtained in the uranium oxide samples resulting from hydrothermal conversion of $U(C_2O_4)_2.nH_2O$ for various temperatures (pH < 1, t = 24 h).

T (°C)	Total weight loss at 1000°C (%)	C (wt.%)	H_2O (wt.%)	H_2O (mol. per unit formula)
180	5.00 ± 0.05	0.82 ± 0.01	4.18 ± 0.05	0.66 ± 0.01
200	2.75 ± 0.05	0.12 ± 0.02	2.63 ± 0.05	0.41 ± 0.01
220	0.80 ± 0.05	0.01 ± 0.03	0.79 ± 0.06	0.12 ± 0.01
240	0.50 ± 0.05	0.02 ± 0.03	0.48 ± 0.06	0.07 ± 0.01
250	0.80 ± 0.05	< 0.01	0.80 ± 0.05	0.12 ± 0.01

Additionally, thermogravimetric experiments were undertaken under inert atmosphere (Ar) to monitor the elimination of residual carbon and to assess the water content in the prepared powders. As expected from the carbon analyses, the sample prepared at 180°C exhibited the highest weight loss (4%). Considering the contribution coming from carbon species, the hydration rate of the sample was then found to be close to 0.7 H_2O per mole of UO_{2+x}. This low value agreed well with the mechanism proposed for the formation of $UO_{2+x}.nH_2O$ samples, i.e. hydrolysis of U(IV) as $U(OH)_4$ after hydrothermal conversion of $U(C_2O_4)_2.nH_2O$, followed by its rapid aging to form hydrated uranium oxide. This dehydration was even more pronounced at 200°C, and led to 0.4 H_2O per formula unit. For higher temperatures of hydrothermal treatment, a very low weight loss, that did not exceed 0.7%, was observed. As the carbon content was almost negligible in these conditions, the mass loss was mainly assigned to water molecule, leading to hydration ratio of about 0.1 H_2O per formula unit. Nevertheless, one must keep in mind that partial reduction of the samples could also occur when heating in highly pure argon atmosphere. In these conditions, the full reduction of $UO_{2.12}$ into $UO_{2.00}$ would also account for a weight loss of about 0.7%. As the dehydration of the oxide sample and its reduction probably process concomitantly, it was then difficult to accurately conclude on the hydration of the sample. Nevertheless, owing to the value determined, the samples could be considered as almost anhydrous.

Effect of initial pH

In order to improve the uranium precipitation yield and to control the morphology of the final powder, a second study was dedicated to the effect of pH value in the starting mixtures. Based on our previous results, the hydrothermal treatment temperature was fixed to 250°C, which corresponded to the samples presenting the lowest O/U ratio as well as the lowest contents of residual carbon and water. The duration of the hydrothermal treatment remained unchanged

(24 hours) while the pH of the starting reacting mixture was fixed to different values between 1 and 10. Monitoring the initial pH of the reacting media quickly led to the quantitative recovery of uranium. Indeed, analyses by PERALS (Photon Electron Rejecting Alpha Liquid Scintillation) undertaken on the supernatants showed that the precipitation yield was close to 100% for pH ≥ 1.

The samples prepared for 1 < pH < 10 were further characterized by PXRD. Whatever the initial conditions tested in terms of acidity, all the diagrams collected matched well with a single fluorite-type structure characteristic of UO_{2+x} oxides or of UO_{2+x} / U_4O_9 mixtures [21]. Once again, no XRD lines splitting, that could sign the formation of U_3O_7, was observed. Also, bringing the pH towards high values then did not lead to stabilize $U(OH)_4$, which systematically aged to form uranium oxide. While previous authors only reported samples prepared close to neutral pH values [40-42], the hydrothermal conversion of $U(C_2O_4)_2.nH_2O$ was then proved to be possible on a wide range of operating conditions.

Although the characteristic XRD lines of the fluorite-type structure were systematically obtained, Rietveld refinements of the PXRD patterns once again revealed that pH variation impacted both the unit cell parameters and the average crystallite size. Conversely to what was observed when studying the effect of hydrothermal treatment temperature, the lattice volume mostly remained in the classical range of variation for UO_{2+x}. For the lowest pH values investigated (*i.e.* up to pH = 1), it was found to be near the reference value reported for $UO_{2.00}$ (V = 163.781 Å^3) [25], therefore indicating that the O/U ratio probably remained close to 2 in such operating conditions. Increasing the pH in the initial reacting media led to favour the uranium oxidization, which was illustrated by the decrease of the unit cell volume. This latter first remained constant around 161.3 Å^3 for 2 ≤ pH ≤ 6, which typically corresponded to UO_{2+x} / U_4O_9 mixtures with a global O/U ratio in the 2.20 - 2.25 range based on the data reported in the literature [30]. In basic media (i.e. for pH = 10), the lattice volume was finally found to be below 161 Å^3, which might indicate an increase of O/U towards higher values, and the presence of U(VI) in the system, as it was observed when studying the effect of the hydrothermal treatment temperature.

In the same time, a strong decrease of the average crystallites size was noted when raising the pH of the reacting media. Indeed, samples prepared around pH = 1 led to crystallite size between 80 and 110 nm while this value drastically dropped down to 20-30 nm for 2 ≤ pH ≤ 5. Such trend could be easily explained by the more rapid uranium (IV) hydrolysis then $U(OH)_4$ precipitation in basic media, which led the crystallites nucleation step to be favoured over the growth processes.

SEM observations were further undertaken and revealed important morphological modifications as a function of the starting pH value (**Figure 7**). At pH = 1, the powders exhibited the morphology already described when working in uncontrolled acidic media, made of submicrometric aggregates of elementary crystallites, even if they appeared to be more faceted. For pH ≥ 2, the samples appeared to be systematically composed of microspheres exhibiting heterogeneous size distribution. Such a morphology was already reported for similar pH values after hydrothermal conversion of uranium(IV) aspartate [37]. This clearly underlined the crucial role played by the pH in the design of morphology-controlled uranium oxides prepared through wet chemistry routes in hydrothermal conditions. The spherical morphology of the powders was further maintained up to pH = 5, although isolated crystallites became more and more visible. Finally, for the higher pH values (typically between 6 and 10), the

powders were found to be mostly composed of elementary nanoscale crystallites. This observation clearly confirmed the rapid hydrolysis of uranium (IV) in basic media, which prevented further growth of the particles and hindered aggregation phenomena. Consequently, the powder was found to exhibit a morphology close to that already described by Martinez *et al.* for uranium dioxide samples prepared through direct hydroxide precipitation [43].

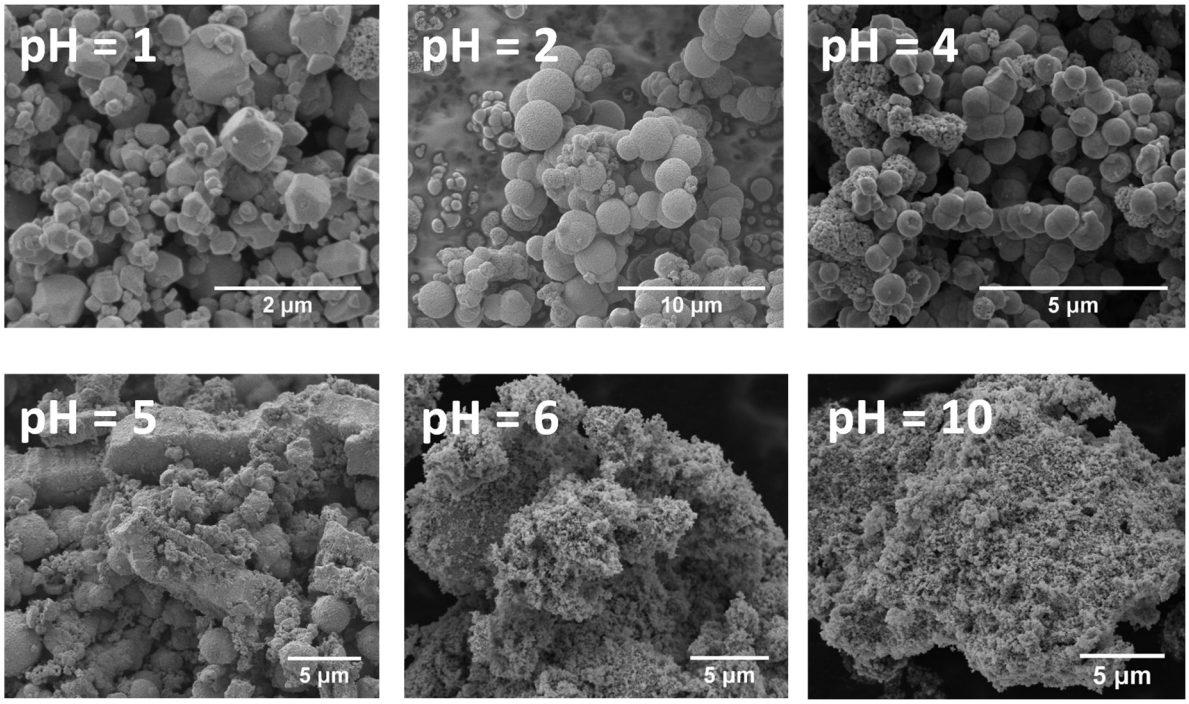

Figure 7. SEM images recorded for samples prepared by hydrothermal conversion of $U(C_2O_4)_2.nH_2O$ (T = 250°C, t = 24h) at various pH.

Finally, the carbon content and hydration rate of the samples were followed by TGA and carbon analyzer. Whatever the conditions considered, the powders only contained limited amounts of impurities (**Table 4**), although it was found to increase with pH. Indeed, whereas very acidic conditions (*i.e.* for pH $\leq$ 1) led to carbon amounts close to 100 ppm, it was found to be one order of magnitude higher between pH = 2 and 10. On this basis, it was probable that the increase of the precipitation kinetics with the pH favoured the carbon trapping within the structure, and/or between the crystallites forming the aggregates. Another explanation could be linked to the presence of carbonate ions in solution following the degradation of oxalate entities. Indeed, regarding to their speciation between pH = 3 and pH = 6, HCO_3^- groups could partially substitute OH^- ions during the precipitation process. Nevertheless, it is important to mention that the carbon amounts measured remained once again close to that obtained after heat treatment of oxalates [9], and far lower than those measured in UO_2 microspheres prepared through wet chemistry processes, which can reach up to 3 wt.% [37, 38]. On the other hand, the water content remained almost constant up to pH = 6 and reached about 0.1-0.2 H_2O per formula unit. Keeping in mind that the associated weight loss could be also linked with a partial reduction of uranium, the samples were then considered as nearly anhydrous. Nevertheless, a strong increase was noted for pH $\geq$ 8, where the hydration rate progressively rose up to one mole of H_2O per mole of uranium. Although this value was still in good agreement with a precipitation mechanism based on the hydrolysis of U(IV), it showed that basic conditions led to slow down the dehydration of the final compound. Also, owing to the high value suspected

This project has received funding from the EURATOM research and training programme 2017-2021 under grant agreement No 755171

for the O/U ratio in this pH range, one cannot exclude the formation of amorphous uranium(VI) oxo-hydroxides such as schoepite[44] in our system, even if they were not evidenced by XRD.

Table 4. Carbon and water contents determined in the samples prepared by hydrothermal conversion of $U(C_2O_4)_2.nH_2O$ (T = 250°C, t =24h) for various starting pH values.

pH	Total weight loss at 1000°C (%)	C (wt.%)	H_2O (wt.%)	H_2O (mol. per unit formula)
< 1	0.80 ± 0.05	< 0.01	0.80 ± 0.05	0.12 ± 0.01
1	< 0.10	< 0.01	< 0.01	< 0.01
2	1.20 ± 0.05	0.09 ± 0.02	1.11 ± 0.05	0.17 ± 0.01
5	1.60 ± 0.05	0.10 ± 0.02	1.50 ± 0.05	0.23 ± 0.01
6	1.55 ± 0.05	0.32 ± 0.02	1.23 ± 0.05	0.19 ± 0.01
8	2.51 ± 0.05	0.07 ± 0.02	2.44 ± 0.05	0.38 ± 0.01
10	5.90 ± 0.05	0.08 ± 0.02	5.82 ± 0.05	0.93 ± 0.01

Effect of hydrothermal treatment duration

Finally, the last set of experiments was dedicated to the impact of kinetics on the physico-chemical properties of the uranium oxide samples resulting from hydrothermal conversion of $U(C_2O_4)_2.nH_2O$. With this objective, the heat treatment was maintained at 250°C while an initial pH value of 5 was chosen to guarantee the quantitative precipitation of uranium, while durations varied from 1 to 48 h.

For all the conditions tested, the obtained powders were found to be crystalline and exhibited XRD lines compatible with the formation of UO_{2+x} oxides or of UO_{2+x} / U_4O_9 mixtures (**Figure 8**). Also, no additional signal, such as that of residual $U(C_2O_4)_2.nH_2O$ was observed, which evidenced its full and rapid conversion in such operating conditions. This agreed well with the data published by Crossey [24]. Indeed, assuming that the activation energy reported in this study (E_A = 207 kJ.mol^{-1}) remained constant up to 250°C, one can determine the kinetic constant associated to the oxalate decomposition, supposed to be a first-order reaction. Such calculations yielded a reaction half-time of about 1.5 minutes at pH = 5. On this basis, the decomposition was considered to be almost complete after 10 periods, i.e. 15 minutes, which corresponds to the conversion of 99.9% of the reactants. In good agreement with these calculations, the uranium precipitation yield was found to be almost complete after one hour of hydrothermal treatment (**Table 5**).

Even though the quantitative precipitation of uranium was reached very rapidly, Rietveld refinements of the PXRD patterns revealed that 5 hours of heat treatment were required to reach a plateau in terms of lattice parameters and average crystallite size. Indeed, after only one hour of heat treatment, the unit cell volume was found to 160.8 Å^3, which accounted for a strongly oxidized system regarding to UO_2. For longer hydrothermal treatment durations, the unit cell volume then increased to reach a constant value of about 162.0 Å^3, which fitted well with the usual range of variation of UO_{2+x} / U_4O_9 lattice parameters. A similar evolution was observed for the crystallite size. It was found that the powders precipitated after only 1 hour of hydrothermal treatment were composed by small crystallites of less than 10 nm in size, which

was only 2 to 3 times higher than that reported by Martinez *et al.* for uranium oxides prepared by direct precipitation of uranium hydroxide at room temperature. Rather than oxalate decomposition, the ageing and growth of $U(OH)_4$ nuclei then could be considered as the main limitation to the preparation of well-crystallized $UO_{2+x}.nH_2O$ powders on such a short time. Conversely, the samples prepared after 5 to 48 hours of heating treatment presented larger crystallite size (i.e. up to 30-40 nm).

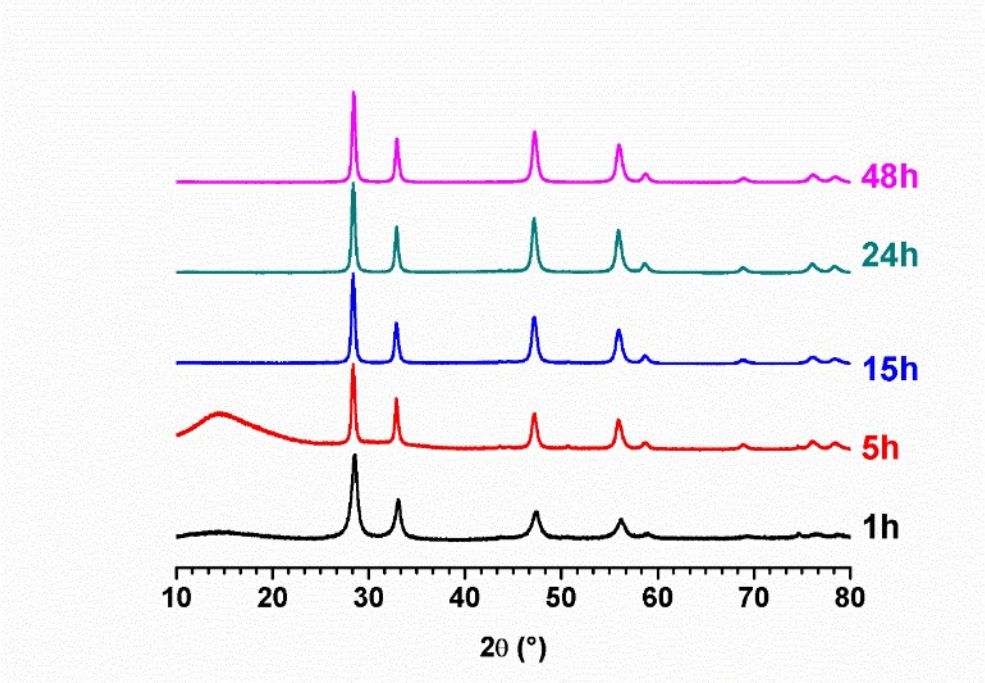

Figure 8. Evolution of the PXRD patterns obtained for samples prepared by hydrothermal conversion of $U(C_2O_4)_2.nH_2O$ (T = 250°C, pH =5).

Table 5. Uranium (IV) precipitation yield measured by PERALS analyses as a function of the heat duration (T = 250°C, pH = 5).

Time (hours)	$n(U)_i$ (mol.)	$n(U)_{sol.}$ (mol.)	Uranium(IV) precipitation yield (%)
1	4.79×10^{-4}	$(1.20 \pm 0.01)\times10^{-5}$	97.5 ± 0.2
5	4.78×10^{-4}	$(2.20 \pm 0.06)\times10^{-7}$	99.9 ± 0.1
15	4.78×10^{-4}	$(4.7 \pm 0.2)\times10^{-7}$	99.9 ± 0.1
24	4.79×10^{-4}	$(1.3 \pm 0.2)\times10^{-7}$	99.9 ± 0.1

The accurate stoichiometry of the samples prepared after 1 and 5 hours of hydrothermal conversion (T = 250°C, pH =5) was then further checked through HERFD-XANES (**Figure 9**). The two samples investigated presented very different spectra. Indeed, after 1 hour of conversion, 4 peaks were clearly visible on the spectrum at 3725.5, 3726.9, 3728.8 and 3732.4 eV. They attested to the presence of both U(IV), U(V) and U(VI) in the sample, including uranyl groups. As the coexistence of all these uranium species was not possible in a single phase, the formation of a polyphase sample was suggested. Conversely, only two main contributions were recorded for the sample prepared after 5 hours of heating, meaning that the amount of U(VI) drastically decreased in the system, which was then mainly composed of U(IV) and U(V).

This project has received funding from the EURATOM research and training programme 2017-2021 under grant agreement No 755171

In order to go further, the O/U ratio in each sample was quantified through a linear combination fitting coupled to the normalization of the uranium amount inside the references used (i.e. UO_2, U_4O_9, U_3O_8 and $UO_2(NO_3)_2.nH_2O$). The results presented in **Table 6** confirmed that the sample prepared after only 1 hour of heat treatment was strongly oxidized with O/U = 2.65 ± 0.14 corresponding to an average uranium oxidation state equal to +5.3. As already suggested, this sample then probably corresponded to a mixture composed by a crystalline UO_{2+x}/U_4O_9 phase (evidenced by XRD) and an amorphous U(VI)-residue. The O/U ratio was further found to decrease after 5 hours of hydrothermal conversion down to 2.45 ± 0.06 ($U^{+4.9}$). One can note that these values remained significantly higher than that determined for heat treatment of 24 hours in more acidic conditions (pH < 1 : O/U = 2.13 ± 0.04).

These results suggested that the hydrothermal conversion of $U(C_2O_4)_2.nH_2O$ could proceed in two distinct steps. The first one would correspond to the oxidative decomposition/dissolution of the oxalate initially precipitated when mixing oxalic acid and U(IV) chloride solution. The oxide formation could then be achieved through the progressive reduction of uranium during the hydrothermal conditions, thanks to the organic moieties generated in solution by the decomposition of oxalates. Indeed, such mechanism was reported for long in geologic media, where uranyl ions were precipitated as UO_2 in late diagenetic conditions (T = 100-200°C) by interacting with simple organic matter [45, 46]. Such a dissolution/precipitation process would explain both the initial formation of a mixture composed by a crystalline U(IV)/U(V) phase and a U(VI) amorphous residue, then the progressive reduction of the oxide sample with time, but also the drastic modification of the sample's morphology compared to the starting square platelets.

Table 6. Uranium oxidation state distribution obtained from the linear combination fitting of HERFD-XANES spectra.

Holding time (h)	U(IV) (%)	U(V) (%)	U(VI) (%)	O/U ratio	Average U oxidation state
1	14.9 ± 0.3	39.6 ± 1.6	45.5 ± 3.1	2.65 ± 0.14	5.3
5	26.5 ± 0.3	57.8 ± 1.6	15.7 ± 0.6	2.45 ± 0.06	4.9

The peculiar behaviour of the sample prepared after only 1 hour of hydrothermal treatment was also confirmed during the determination of carbon and water contents. Indeed, the residual carbon amount was found to be close to 10 000 ppm, which was by far the highest value measured during this study. Nevertheless, it dropped down to 500-1000 ppm when extending the hydrothermal treatment to 5 - 48 hours. The organic species coming from the initial decomposition of oxalate groups, which played an important role in the reduction of uranium, were then probably trapped during the formation of the first oxide nuclei, then were quickly and efficiently eliminated throughout the hydrothermal treatment. Simultaneously, the water content also decreased, going from about 0.7 H_2O per formula unit after 1 hour to 0.1 - 0.2 after 5 to 48 hours. Along with the carbon elimination, the crystallization of uranium oxide was then also accompanied by the partial dehydration of the samples.

This project has received funding from the EURATOM research and training programme 2017-2021 under grant agreement No 755171

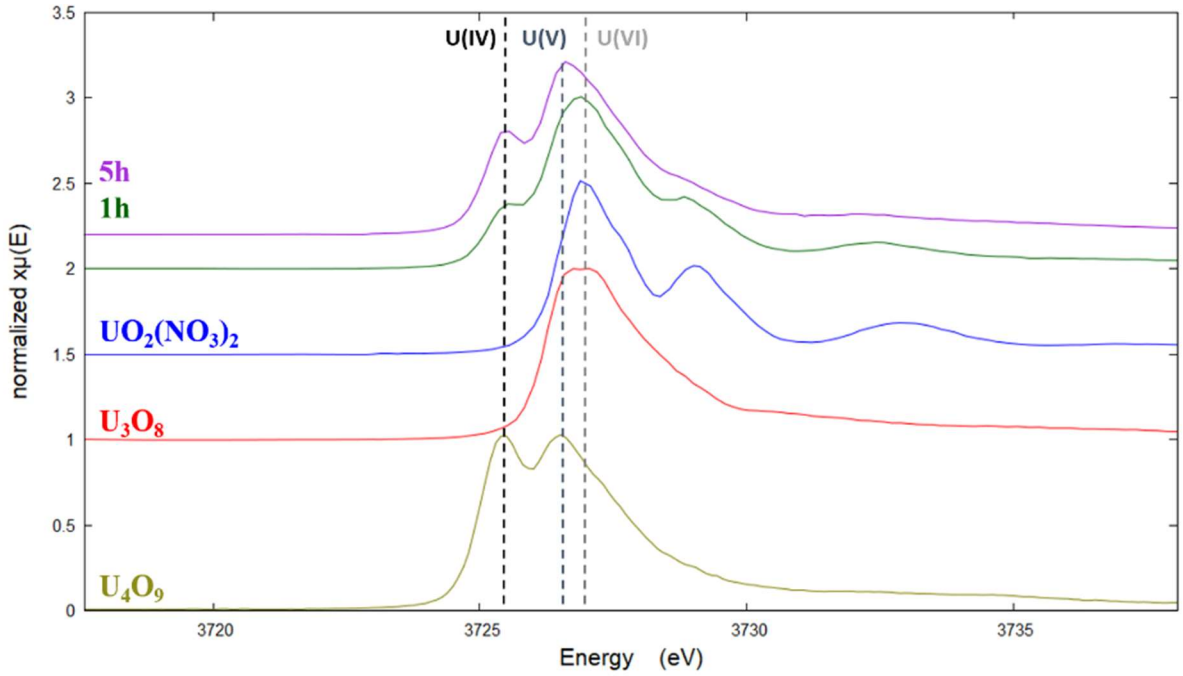

Figure 9. Normalized HERFD-XANES spectra of reference samples and of oxide samples obtained after hydrothermal treatment of $U(C_2O_4)_2.nH_2O$ at 250°C and pH = 5 for various durations.

Extension to $(U,Ce)O_{2\pm\delta}$ mixed oxides

In order to envisage the preparation of $(U,Pu)O_2$ MOx or of advanced fuels incorporated minor actinides such as americium, the synthesis of $U_{1-x}Ce_xO_{2\pm\delta}$ solid solutions through the hydrothermal conversion of oxalate precursors was also studied. With this aim, the optimal temperature of 250°C was maintained, with a duration of 24 hours. Besides, starting pH was raised to 8 in order to allow the quantitative hydrolysis of Ce^{3+}. Finally, the total concentration in cations was set to 2.6 10^{-2} M, with cerium mole ratio equal to x = 0.10, 0.25 and 0.50.

The initial precipitate formed through the mixture cerium (III), uranium (IV) and oxalic acid was first characterized by XRD (**Figure 10**). The pattern collected evidenced the characteristic diffraction lines of the hexagonal structure of mixed M^{III}/M^{IV} oxalate. By comparison with the previous study reported by Mudher *et al.* and the PDF 00-053-0421 reference, the initial precursor was then identified as $(NH_4)Ce^{III}_xU^{IV}_{1-x}(C_2O_4)_4,8H_2O$ solid solutions [47].

The XRD patterns of the samples obtained after hydrothermal conversion of the precursors are gathered in **Figure 11**. All the patterns evidenced the characteristic XRD lines of the fluorite-type structure shared by UO_2 and CeO_2. Moreover, no splitting of the XRD peaks was observed, indicating that the solid phase was closer to a solid solution than to a mixture of oxides. Also, it is important to underline that the use of Ce(III) nitrate as a starting reagent did not yield to any significant oxidation of uranium(IV), as no traces of U_4O_9 or U_3O_8 were detected in the patterns collected.

This project has received funding from the EURATOM research and training programme 2017-2021 under grant agreement No 755171

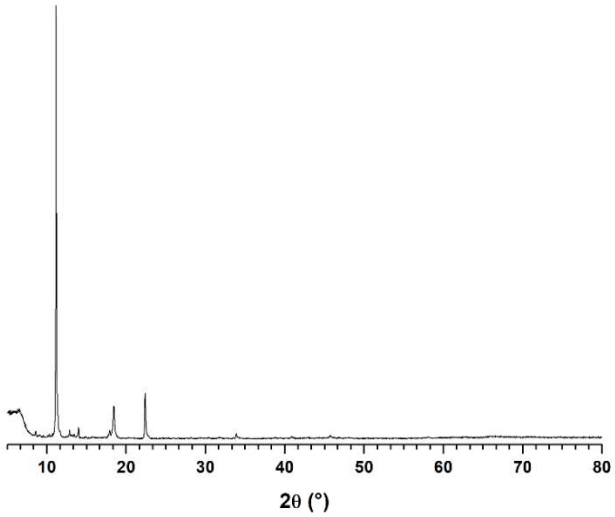

Figure 10. XRD pattern of the samples obtained after adding equimolar mixture of cerium (III) and uranium (IV) to oxalic acid (total cation concentration of $2.6 \cdot 10^{-2}$ M, pH = 8).

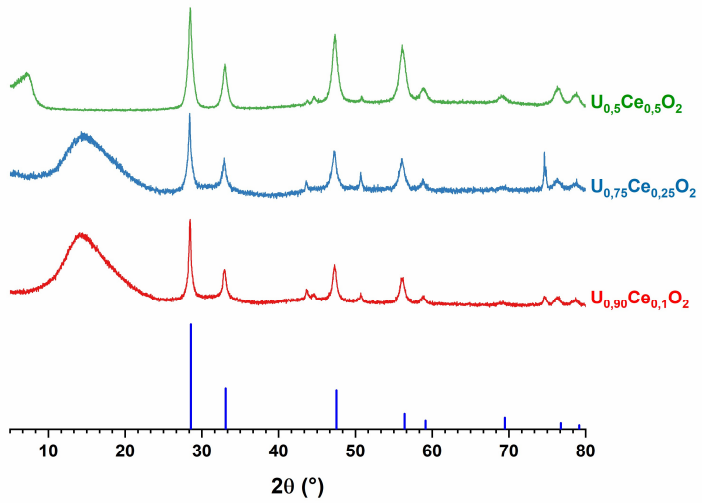

Figure 11. XRD patterns of $U_{1-x}Ce_xO_2$ oxides after hydrothermal treatment at 250°C and pH = 8 during 24h. Blue lines indicate the reference XRD pattern of CeO_2.

SEM-EDS analyses then allowed the determination of the chemical composition of the samples prepared. The data gathered in **Table 7** show that the final oxide composition generally differed from the initial U/Ce mole ration. Indeed, the cerium precipitation appeared to be quantitative only for x = 0.10, while the oxides only incorporate 11.5 ± 1.8mol.% and 19.1 ± 2.7mol.% in cerium when composition of x = 0.25 and x = 0.50, respectively, were targeted. The origin of this deviation was assigned to a difference in the kinetics of oxalate decomposition process. Indeed, preliminary tests showed that cerium (III) oxalate hydrothermal conversion went through numerous intermediates before yielding to oxide. Additional tests with increased duration of hydrothermal treatments then must be considered to reach the desired composition. Nevertheless, although the targeted composition was not obtained, it is important to underline that small deviation were associated to the elementary mole percentages, which might indicate a good homogeneity of the powders.

This project has received funding from the EURATOM research and training programme 2017-2021 under grant agreement No 755171

Table 7. Composition of $U_{1-x}Ce_xO_2$ prepared though hydrothermal conversion of oxalate precursors (T = 250°C, t = 24h, pH = 8), as determined by SEM-EDS analyses.

$x_{calc.}$	%mol. U	%mol. Ce
0.10	90.3 ± 1.3	9.7 ± 1.3
0.25	88.5 ± 1.8	11.5 ± 1.8
0.50	80.9 ± 2.7	19.1 ± 2.7

Conclusion

Mixtures of uranium oxides, with a typical O/U ratio ranging from 2.12 to 2.65, were obtained by hydrothermal conversion of $U(C_2O_4)_2 . nH_2O$ in various operating conditions. In very acidic media (i.e. for pH ≤ 1), the lowest temperatures explored (typically from 180 to 200°C) led to O/U ratio of 2.38 ± 0.10 while the XRD pattern did not present any characteristic reflections of U_3O_7 or U_3O_8. A similar XRD pattern, typical for UO_{2+x} or UO_{2+x}/U_4O_9 mixtures was further obtained for samples prepared between 220 and 250°C, while O/U was lowered to 2.13 ± 0.04. The use of hydrothermal conditions, combined with the nanocrystalline nature of the powders then allowed to stabilize mixtures of cubic uranium oxide phases, which cannot be uniquely distinguished from XRD alone, while XANES results indicated an important U(V) contribution in some powders. In parallel, increasing the temperature of the hydrothermal treatment efficiently improved the elimination of residual carbon species. Typical amounts of about 100-200 ppm were measured in the samples, which was of the same order of magnitude than the values usually observed when performing thermal conversion of An (IV) oxalates in air. Additionally, high temperature of hydrothermal treatment was also found to yield almost anhydrous samples.

Hydrothermal conversion of $U(C_2O_4)_2.nH_2O$ also led to the drastic modification of the powders morphology. With this aim, pH monitoring could be used to shift from bipyramidal aggregates (up to pH = 1), microspheres (2 ≤ pH ≤ 5) and finally to nanometric powders (pH > 5). However, the increase of the kinetics of U^{4+} hydrolysis with the pH value led to enhance the amount of carbon trapped in the samples, even if this latter remained of the same order of magnitude than that reported for uranium (IV) oxalate heated under reducing atmosphere.

Finally, the kinetics of the hydrothermal conversion suggested a two-step mechanism for the transformation of uranium (IV) oxalate into oxide. Indeed, if the complete decomposition of the initial oxalate was achieved in only few hours, the O/U ratio in the samples appeared to be strongly impacted by the duration of the hydrothermal treatment. After 1 hour, it suggested the existence of a U(VI)-bearing secondary phase, such as amorphous UO_3, aside the crystalline UO_{2+x}/U_4O_9 mixture, which further tended to reduce to UO_{2+x}. The hydrothermal conversion was then likely to be composed of an oxidative dissolution of the initial precursor, followed by the *in situ* reduction of U(V) and/or U(VI) in solution thanks to organic species and the final hydrolysis process leading to the oxide sample.

By these means, hydrothermal conversion of oxalates appeared as an easy and efficient way to yield highly pure uranium oxide samples in solution. The absence of impurities as well as the possibility to monitor the samples morphology also paved the way to the direct sintering of the powders prepared. Avoiding the thermal conversion of oxalate will then give the opportunity to set up dustless processes that will convert ions in solution to sintered pellets in a limited number of steps.

This project has received funding from the EURATOM research and training programme 2017-2021 under grant agreement No 755171

With the aim of controlling more precisely the final morphology of the oxide powders produced under hydrothermal conditions, the study was moved toward the conversion of complex involving amino acids. Aspartic acid was chosen as precipitating agent owing to its good complexation properties with regard to actinides [48, 49]. Also, it readily decomposed under hydrothermal conditions, mainly through deamination [50]. Aspartic acid (1 – 1.5 mmol) was first weighted and dissolved in 10 mL H_2O. The pH of the resulting solution was raised to 2 by addition of 30% NH_4OH. The uranium (IV) chloride solution (0.5 mmol) was then added dropwise, while controlling the pH with ammonia. The mixture of solutions rapidly led to the formation of a greenish precipitate. The concentration of uranium remaining in the supernatant was analysed by Photo-Electron Rejecting Alpha Liquid Scintillation (PERALS) [51] and revealed quantitative precipitation.

Afterwards, both solid phase and supernatant were transferred into a Teflon-lined autoclave (Parr) and treated hydrothermally at 160°C for 1 to 30 hours. For several tests, the reacting media were agitated during hydrothermal treatment using a magnetic stirrer (2Mag – MixControl 20). This setup was chosen to be close to the unbaffled stirred tank reactors envisaged for precipitation reactions in nuclear fuel reprocessing industry [52]. Whatever the operating conditions, the autoclave was cooled down overnight before collecting the final precipitate. This latter was separated by centrifugation, washed twice with deionized water and twice with ethanol, and finally dried overnight at 60°C.

Effect of pH

With the aim to obtain uranium oxide powders and to orientate their morphology, the hydrothermal conversion of the amorphous U(IV) aspartate precursors was undertaken. Recent studies showed that mild hydrothermal conditions induced the decomposition of actinide carboxylates, such as uranium(IV) oxalate, leading to the direct formation of UO_2 in solution [53]. As this latter result from the hydrolysis of U^{4+} after the initial decomposition of the precursor, the pH of the solution has to be carefully controlled. Preliminary tests were undertaken to determine the optimal acidity of the reacting media. For pH ≥ 3, SEM micrographs revealed that the precipitates consisted of strongly agglomerated sub-micrometric particles (**Figure 12**), which probably formed through the fast nucleation of $U(OH)_4$ and further aging as partly amorphous UO_2. Indeed, Rai *et al.* already reported that such a compound readily precipitated at pH > 2 and at room temperature [54], while the solubility of amorphous UO_2 did not sustain important variation up to 300°C [13]. For more acidic conditions, *i.e.* for pH = 1 and 2, some grains presenting a spherical habit were systematically obtained. However, they appeared to be denser and monodisperse (although significantly smaller) for pH = 2. This condition was then retained for the rest of our study. Similarly, we decided to maintain the temperature at 160°C in accordance with the protocol originally designed for the thorium counterpart [55]. In order to optimize the operating parameters, a multi-parametric study combining the effects of heating time at 160°C, of initial metal/ligand ratio and of magnetic stirring was then undertaken.

This project has received funding from the EURATOM research and training programme 2017-2021 under grant agreement No 755171

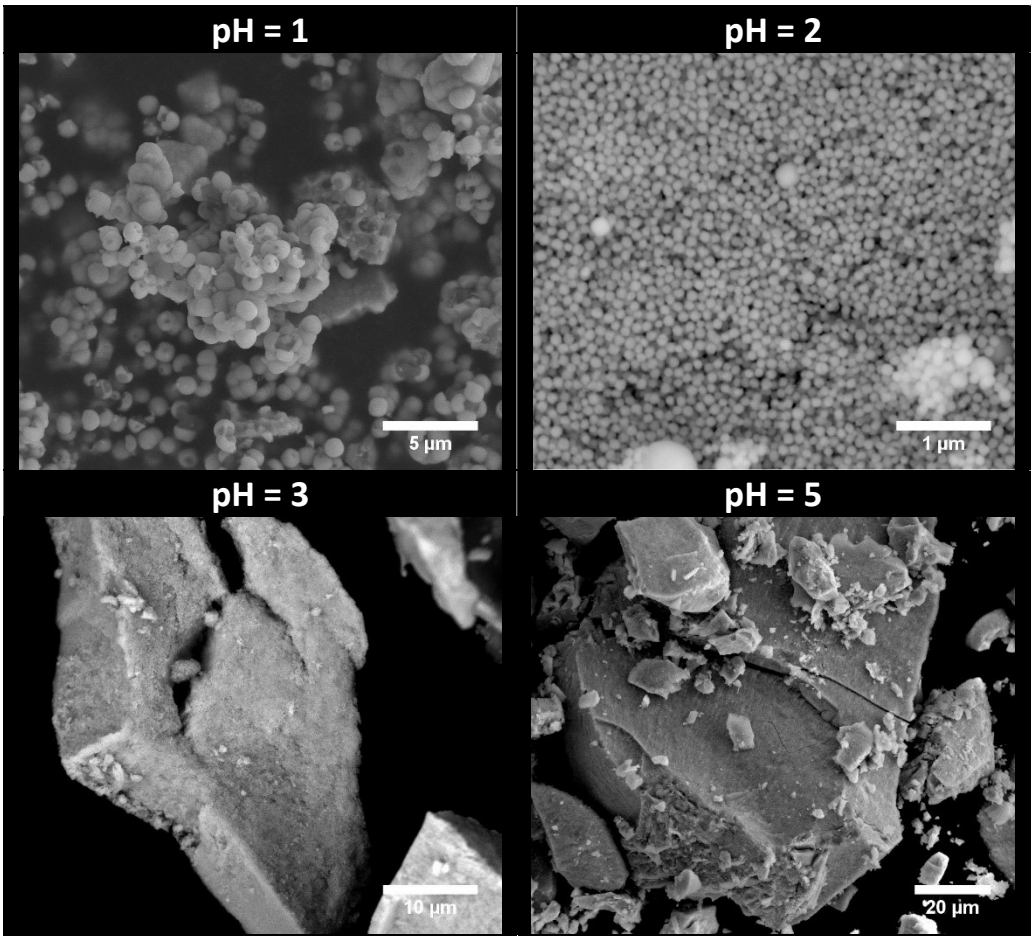

Figure 12. SEM micrographs of the powders obtained after hydrothermal conversion of uranium(IV) aspartate at 160°C for different pH.

Effect of heating time

First, the hydrothermal treatment at 160°C was extended from 1 to 30 hours. For all the holding times considered, the supernatant was analysed by PERALS [51] to quantify the concentration of uranium remaining in solution (**Table 8**). The uranium precipitation yield was found to increase slightly during the first hours of hydrothermal treatment, uranium precipitation becoming quantitative after heating over 24 hours. On this basis, the beginning of the hydrothermal treatment (*i.e.* up to 6 hours) probably still corresponded to the decomposition of the initial U(IV) aspartate precursor, followed by the partial hydrolysis of the tetravalent uranium in solution. This observation was in very good agreement with the data reported by Faisal *et al.* concerning the decomposition of aspartic acid under hydrothermal conditions [56]. These authors stated that the main reaction pathway consisted in an irreversible deamination yielding malic acid, followed by a possible decarboxylation leading to a mixture of pyruvic and lactic acids:

$$\underset{\text{Aspartic acid}}{C_2H_3(NH_2)(COOH)_2} \xrightarrow{-NH_3} \underset{\text{Malic acid}}{C_2H_3(OH)(COOH)_2} \xrightarrow{-CO_2} \underset{\text{Pyruvic acid}}{CH_3(CO)(COOH)} \xrightarrow{+H_2O} \underset{\text{Lactic acid}}{C_2H_4(OH)(COOH)} \quad \textbf{(2.)}$$

Moreover, based on their determination of kinetic constants at 200°C and of the activation energy associated with the decomposition reaction (E_A = 144 kJ.mol^{-1}), the time required to

This project has received funding from the EURATOM research and training programme 2017-2021 under grant agreement No 755171

decompose 99% of initial aspartic acid can be estimated to be about 5.5 hours at 160°C. Shorter heating times then should be discarded if one wanted to quantitatively recover U^{4+} from the decomposition of the aspartate precursor in these operating conditions.

Table 8. Determination of the uranium precipitation yield from PERALS analyses for various durations of hydrothermal process (T = 160°C).

Heating time (hours)	n(U) initial (mol.)	n(U) supernatant (mol.)	Uranium precipitation yield (%)
0	5.55×10^{-4}	$(1.1 \pm 0.1) \times 10^{-5}$	98 ± 1
1	4.77×10^{-4}	$(6.0 \pm 0.1) \times 10^{-5}$	87 ± 2
3	4.78×10^{-4}	$(3.48 \pm 0.07) \times 10^{-5}$	93 ± 2
6	4.78×10^{-4}	$(1.68 \pm 0.02) \times 10^{-5}$	96 ± 1
24	4.77×10^{-4}	$(0.23 \pm 0.01) \times 10^{-5}$	99 ± 2
30	4.78×10^{-4}	$(0.34 \pm 0.01) \times 10^{-5}$	99 ± 2

Concomitantly to the increase of the uranium precipitation yield, powder morphology appeared to be strongly modified when increasing the duration of the hydrothermal process. After 1 hour, the morphology was very close to that observed for the aspartate precursor, with a powder composed by sub-micrometric crystallites (**Figure 13**). This was still found to be the major habit observed between 6 and 24 hours of hydrothermal treatment, but some scarce spherical grains tended to form. After 30 hours, the morphology of the sample drastically changed. The powder was composed of spherical grains with variable sizes, typically ranging from 200 nm to 1 µm in diameter. On this basis, the operating conditions for the hydrothermal treatment were fixed to 30 hours and T = 160°C for all the following experiments.

The changes observed in the morphology of the samples were also associated to structural modifications. Whatever the conditions chosen, the XRD patterns collected present low-intensity and wide peaks characteristic of poorly crystallized and/or nanosized samples, in good agreement with the SEM observations (**Figure 14**). Despite the low resolution of the XRD patterns, it was still possible to note an evolution of the structure along the hydrothermal treatment. For samples heated between 1 and 3 hours, the XRD pattern was very close to that previously reported for thorium aspartate [55]. Compared with the NMR data, which rather suggested the initial precipitation of an amorphous uranium (IV) aspartate coordination polymer, this result indicated that a transformation towards a molecular specie probably occurred during the first hours of heat treatment at 160°C. Under these conditions, short hydrothermal treatment did not allow to convert the precursor into oxide, but only resulted in the transformation and partial crystallization of the initial precipitate. Conversely, after 6 hours of heating at 160°C and for longer hydrothermal treatments, the characteristic XRD pattern of nanosized fluorite-type UO_2 was evidenced [43] while the peaks of the U(IV) aspartate were no longer observed. This suggested the full conversion in these operating conditions and again appeared in good agreement with previous studies dedicated to aspartic acid decomposition under hydrothermal conditions [56]. Moreover, the width of the XRD lines was not significantly modified over the time, meaning that the average crystallite size remained almost unchanged. The spherical particles observed after 30 hours of hydrothermal processing were thus formed by smaller entities, resulting in a hierarchical structure [38].

This project has received funding from the EURATOM research and training programme 2017-2021 under grant agreement No 755171

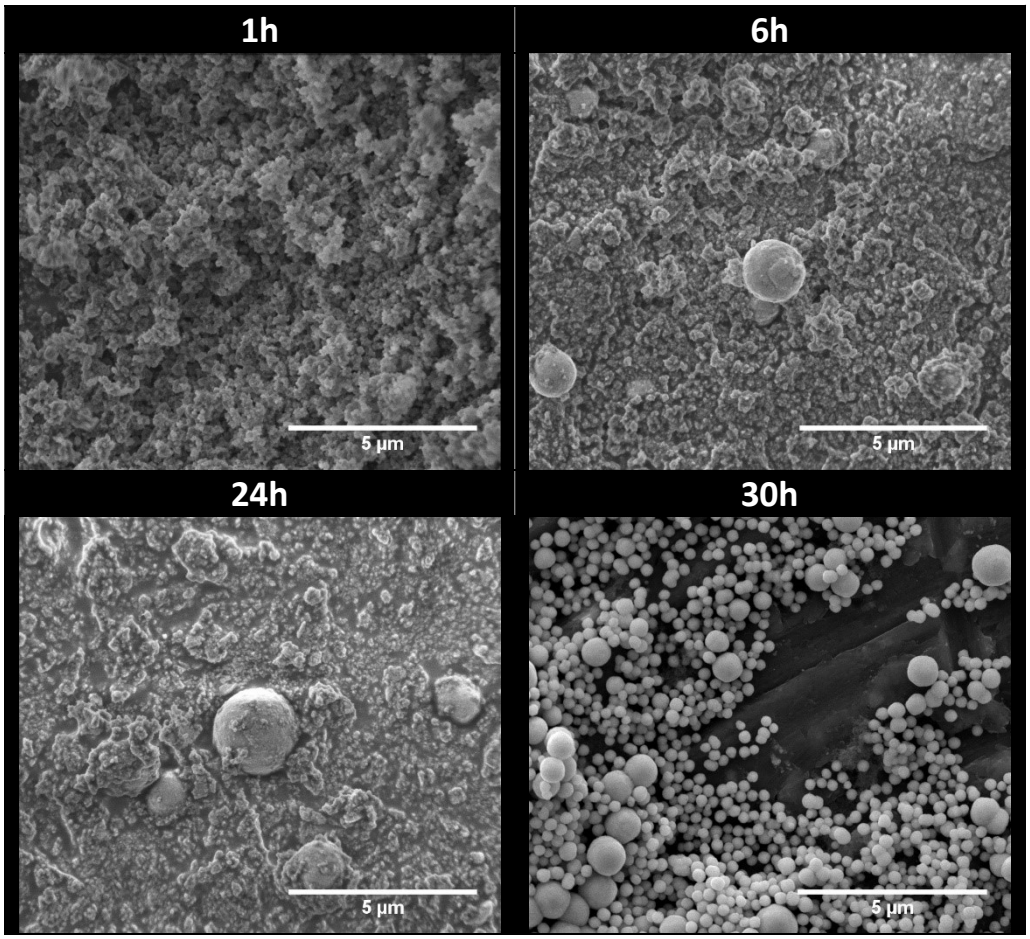

Figure 13. SEM micrographs of the powders obtained after hydrothermal conversion of uranium (IV) aspartate at 160°C for different durations.

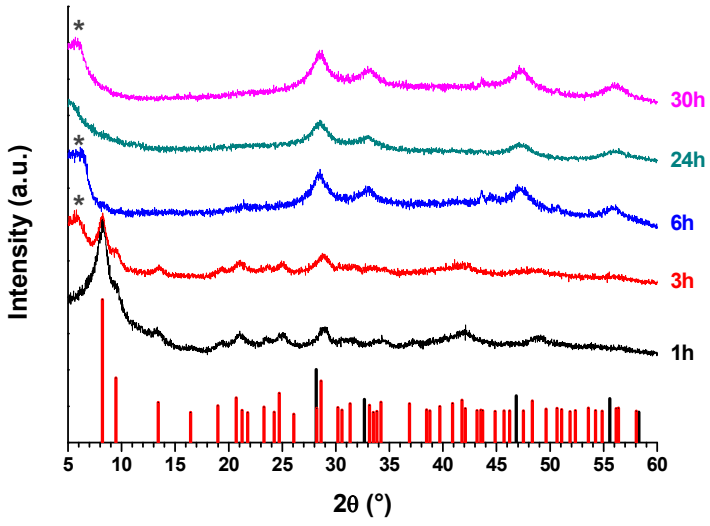

Figure 14. XRD patterns of the samples obtained after hydrothermal conversion of uranium (IV) aspartate at 160°C for various durations. XRD lines of thorium aspartate (red) [55] and UO_2 (black, ICDD #01-071-4823) are supplied for comparison. * Symbols indicate the signal due to anti-contamination dome-shaped container.

This project has received funding from the EURATOM research and training programme 2017-2021 under grant agreement No 755171

Effect of uranium / aspartic acid stoichiometry

As the organics resulting from the hydrothermal decomposition of the uranium (IV) aspartate precursor could play a role in the oxide's final morphology, the metal / ligand molar ratio (*i.e.* uranium / aspartic acid molar ratio) in the initial reacting media was varied in order to evaluate the influence on particle shape and size distribution. First, hydrothermal treatment of the U(IV) chloride solution was performed at pH = 2 without any addition of aspartic acid. In such operating conditions, a small amount of precipitate was obtained after heating for 30 hours at 160°C. It exhibited wide XRD peak characteristics of the UO_2 fluorite-type structure, confirming that the hydrolysis of U^{4+} was the key-step in the formation of an oxide precipitate. Nevertheless, the powder appeared to be composed of very small grains (**Figure 15**), comparable to the nanoparticles obtained from synthesis via precipitation of hydroxides [43].

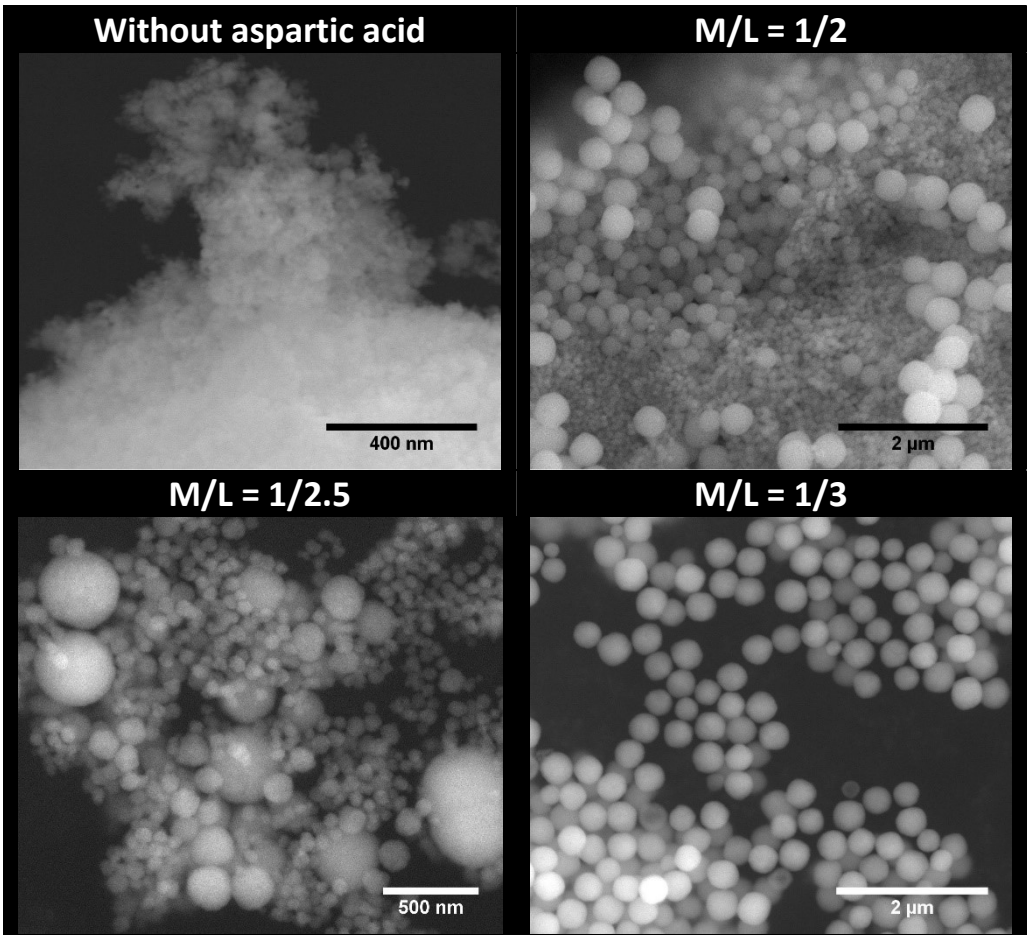

Figure 15. SEM micrographs of the powders obtained after hydrothermal conversion of uranium (IV) aspartate (T = 160°C; t = 30 hours) for different metal / ligand ratios.

On the other hand, the introduction of aspartic acid in the reactant mixture, leading to the formation of uranium (IV) aspartate precursor, was systematically associated with the formation of spherical UO_2 particles whatever the initial content considered. The residual organic molecules detected in the final oxide particles then probably acted as stabilizing agent in the orientation of the sample's morphology towards spheres. Nevertheless, the M/L molar ratio appeared to strongly impact the size distribution of the particles. Indeed, for stoichiometric conditions (*i.e.* M/L = 1/2, based on the initial precipitation of $U(C_4NO_4H_5)_2 \cdot nH_2O$) and for an

excess of 25% (M/L = 1/2.5), the powder was found to be polydisperse. The powders were composed of a large population of small particles (typically between 20 and 150 nm in diameter) but included some larger spheres up to 700 nm in diameter. These latter did not account for a large number of particles but represented the main part of the volume. On the other hand, an excess of 50% in aspartic acid (i.e. M/L = 1/3) led to a very homogeneous powder. The statistical analysis of the particles showed that the size distribution basically followed a Gaussian law, associated to an average diameter of about 380 nm, and a FWHM of about 60 nm. Owing to a dispersion less than ± 10%, the powder was considered as monodisperse. One can also note that increasing the initial excess in aspartic acid increased the average diameter of the main particle population, typically from around 100 nm for stoichiometric conditions to about 400 nm for a 50 mol.% excess. On this basis, a molar ratio of 1/3 between uranium (IV) and aspartic acid was considered for the rest of the study in order to recover samples with an homogenous particle size.

Effect of magnetic stirring

In a last step, magnetic stirring was applied during the hydrothermal treatment with the aim to drive the aggregation of the crystallites towards spherical particles, and to get an accurate control over the final size of the particles. In order to accurately quantify the effects of stirring through a dimensionless number, and to characterize the flow in the reactor as laminar or turbulent, the impeller Reynolds number (derived from the conventional Reynolds number used to describe flow in pipes) was determined for each stirring speed studied in the range 200-1100 rpm as follows:

$$Re_a = \frac{N \times D^2}{\nu} \qquad (3.)$$

Where N is the impeller (stirrer bar) rotation speed, D the stirrer bar length and v the kinematic viscosity. Herein, we assimilated the liquid media to pure water and extracted the viscosity value from the study of Deguchi *et al.* with $\nu \approx 1.8 \times 10^{-7}$ $m^2.s^{-1}$ at 160°C [57]. The stirrer bar length (12 mm) was chosen to be about half the diameter of the reactor (25 mm) in order to create two mixing zones, *i.e.* free and forced vortexes, as described by Bertrand *et al.* [22]. On this basis, smooth stirring up to N ≈ 200 rpm corresponded to $Re_a < 2000$ characteristic of a laminar flow. In this case, the particles size increased from about 400 nm (no stirring) to 1200 nm (**Figure 16a**), meaning that the establishment of a laminar flow in the reactor likely acted in favour of the agglomeration of the elementary crystallites.

Between 200 and 800 rpm (*i.e.* $2000 < Re_a < 10000$), the average particles diameter was found to stabilize between 1.5 and 2 µm. However, the size distribution appeared to be very wide, meaning that polydisperse powders were obtained due to the establishment of a transition regime between laminar and turbulent flows. Finally, higher agitation speeds led to $Re_a > 10^4$, characteristic of turbulent flow. In this case, a clear linear relationship was established between Re_a (stirring speed) and the average diameter of the spherical UO_2 particles (**Figure 16b**). Indeed, the size of the particles was found to decrease from around 2500 nm to 400 nm when the stirring speed increased in the 900 - 1100 rpm range. In this case, the interactive force assembling the crystallites as spherical particles was surpassed by the turbulent shear stress. Growth of the particles was then hindered even though aggregation of the crystallites was favoured by the increase of agitation speed [58]. Lastly, one must note that three different

This project has received funding from the EURATOM research and training programme 2017-2021 under grant agreement No 755171

batches were prepared at 950 rpm (Re_a = 12000) to check the reproducibility of the process developed. In these conditions, all the powders exhibited very similar average particle diameters (i.e. 1340 ± 65, 1390 ± 80 and 1410 ± 50 nm) which confirmed the accuracy of the size control provided by the magnetic stirring during the hydrothermal conversion.

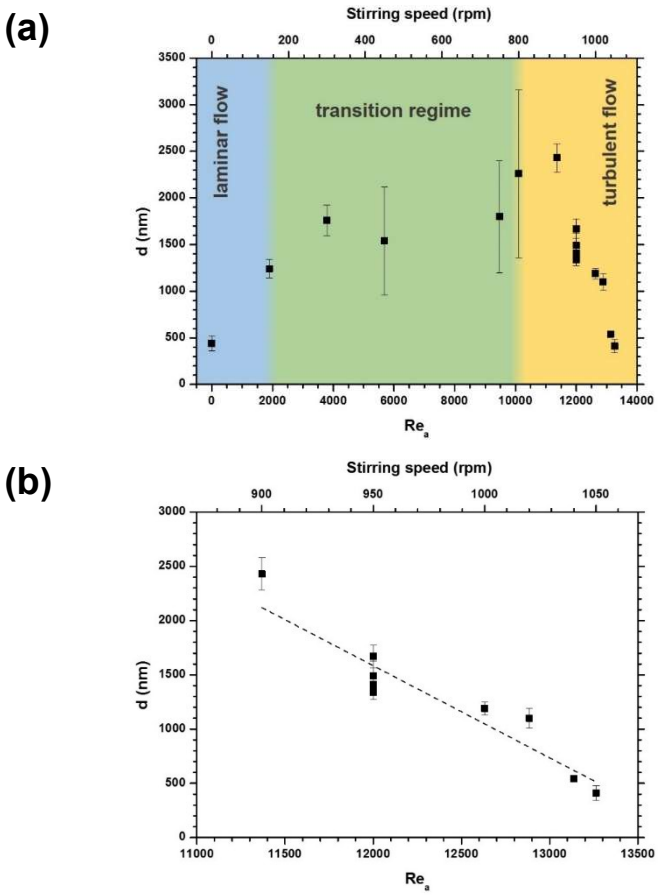

Figure 16. Variation of the average diameter of UO_2 spherical particles versus the impeller Reynolds number and corresponding magnetic stirrer speed (a), and focus on the turbulent flow region (b) (T = 160°C; t = 30 hours; M/L = 1/3).

Conclusion

An easy wet chemistry route was designed to prepare submicrometric spherical UO_2 particles through the hydrothermal conversion of uranium (IV) aspartate. An initial amorphous precursor was obtained by mixing uranium (IV) chloride with aspartic acid, resulting in quantitative precipitation. The conversion towards UO_2 precipitates was then operated *via* heat treatment under mild hydrothermal conditions at T = 160°C. A multiparametric study then allowed us to specify the operating conditions leading to monodisperse and size-controlled particles. Hydrothermal treatment of 6 hours was found necessary to completely convert the precursor into dioxide. Moreover, additional heating up to 30 hours appeared to be mandatory in order to recover only spherical particles. Their size distribution appeared to be driven by the content of organics in the solution, *i.e.* by the initial uranium/aspartic acid molar ratio. On this basis, a minimal excess of 50 mol.% in ligand (M/L = 1/3) was required to obtain monodisperse powders, with a typical variation of about ±10% on the average diameter. Finally, it was

This project has received funding from the EURATOM research and training programme 2017-2021 under grant agreement No 755171

possible to control the particle size by applying magnetic stirring during the hydrothermal treatment. In a turbulent flow regime, *i.e.* impeller Reynolds number above 10^4, a linear variation of the particle diameter versus the stirring speed was observed, with size ranging from 400 nm (1050 rpm) to 2500 nm (900 rpm), which paved the way to applications of such materials in various scientific areas. Also, the protocol was found to be robust and reproducible, with only very limited particle size variation from one batch to another.

Such one-pot wet chemistry route appears to be very promising for the production of spherical UO_2 particles and can be simply implemented in any nuclear chemistry lab. Additional experiments are now under progress to extend this methodology to other systems of interest, including mixed-oxides such as $(U,Ce)O_2$ and $(U,Ln^{III})O_{2-x}$.

This project has received funding from the EURATOM research and training programme 2017-2021 under grant agreement No 755171

DENSIFICATION OF HOMOGENOUS $(U,Ce)O_{2\pm\delta}$

To first produce dense and homogenous pellets, which can be used during dissolution tests, highly homogeneous $U_{1-x}Ce_xO_{2\pm\delta}$ oxides ($0.1 \leq x \leq 0.5$) prepared by hydroxide precipitation and further heat treatment at 700°C were sintered. A dilatometric study first evidenced the very high sintering capability of the powders, with densification temperatures lowered by 100 to 200°C compared to those used for the MOX fuel elaboration. Moreover, it allowed us to master the microstructure of samples with high relative densities (typically above 95%TD) and grains sizes going from few hundreds of nanometers to several tens of micrometers depending on the conditions used (temperature, atmosphere). This study showed that the sintering atmosphere had a big impact on the sintering process, with higher grain size obtained when working under Ar atmosphere compared to reducing conditions (**Figure 17**). To understand such behaviour, XANES measurements were performed to follow the speciation of both uranium and cerium in the materials. It revealed that nearly stoichiometric compounds were obtained in reducing atmosphere whereas inert atmosphere drove to oxidized compounds. This results clearly showed the redox interplay between uranium and cerium during the sintering process at high temperature, and then underlines the need to master the homogeneity of the cation distribution during the preparation of the starting powders.

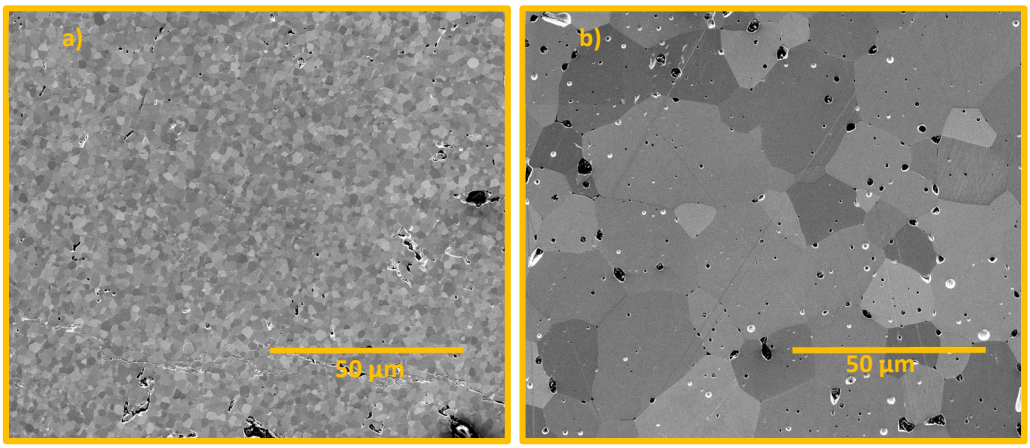

Figure 17. SEM micrographs of $(U_{0.86}Ce_{0.14})O_{2\pm\delta}$ pellets sintered at 1600°C under Ar/H_2 4% (a) or Ar (b) atmosphere.

With this aim, wet chemistry methods appeared as powerful tools to produce homogenous samples. Nevertheless, if the preparation of nanosized powders was definitely an asset to reach low sintering temperatures, it could be considered to be penalizing in an industrial process due to radiotoxicity and dissemination issues. On this basis, the next sections will be dedicated to the sintering of powders obtained through the hydrothermal conversion of carboxylate precursors, which have been shown to produce micro-sized powders with controlled morphology, yet composed of nanometric crystallites.

This project has received funding from the EURATOM research and training programme 2017-2021 under grant agreement No 755171

Selection of samples and operating conditions

According to the results of the study dedicated to the hydrothermal conversion, the pH of the initial solution appeared to the experimental parameter that was the most prompt to impact the sintering behaviour of the powders. It mostly arose from the samples morphology which effect has been studied in details. In this purpose, three uranium oxide samples prepared at 250°C for 24 hours at different pH were selected, with their characteristics summarized in **Table 9**.

Table 9. Characteristics of uranium oxide powders prepared at 250°C for 24 hours selected for the sintering study.

pH	Average crystallites size (nm)	Specific surface area ($m^2.g^{-1}$)	Morphology	Residual carbon content (mass.%)	Hydration rate (mol. H_2O / U)	O/U ratio range	Average green density (%)
1	80 - 110	2.6 ± 0.1	Single crystals	< 0.01	< 0.01	2.00-2.05	56.2 ± 1.2
2	20 - 30	14.5 ± 0.1	Microspheres	0.09 ± 0.02	0.17 ± 0.01	2.20-2.25	48.1 ± 1.3
8	10	29.9 ± 0.1	Nano-powders	0.07 ± 0.02	0.38 ± 0.01	2.20-2.25	52.6 ± 1.2

The sample synthesized at pH = 1 was composed of polyhedral grains ranging from 100 nm to almost 1 µm in length. This size lied in the same order of magnitude than that of the average crystallite sizes determined from Rietveld refinement of XRD data, meaning that most of the particles were considered as single crystals. As a consequence, the associated specific surface area was found to be very low, *i.e.* 2.6 ± 0.1 $m^2.g^{-1}$ (**Figure 18**). At pH = 2, the powders were found to be mainly composed of polydisperse spherical particles of 500 nm to 5 µm in diameter. Similar particles were already described during the hydrothermal treatment of other uranium (IV) carboxylates in a comparable range of pH [37]. They were composed by smaller crystallites of 20-30 nm and still bore an important porosity, which led to a specific surface area of 14.5 ± 0.1 $m^2.g^{-1}$. Finally, the powder prepared at pH = 8 appeared in the form of loose nanoparticles of approximately 10 nm in size, leading to the highest specific surface area of this set of samples (29.9 ± 0.1 $m^2.g^{-1}$). As a result, the samples prepared at pH = 1, 2 and 8, will be referred to as single crystals, microspheres and nano-powders, respectively. Regarding impurities, the powder obtained at pH = 1 only presented negligible traces of carbon (typically less than 100 ppm) and water, whereas carbon content was close to 0.1 wt.% for the other two powders. At the same time, the hydration rate increased up to around 0.4 H_2O per mole of uranium for powders synthesised at pH = 8. Moreover, single crystals showed a very short deviation from the stoichiometry with the O/U ratio estimated to less than 2.05 whereas the other two morphologies showed an O/U ratio higher than 2.20.

This project has received funding from the EURATOM research and training programme 2017-2021 under grant agreement No 755171

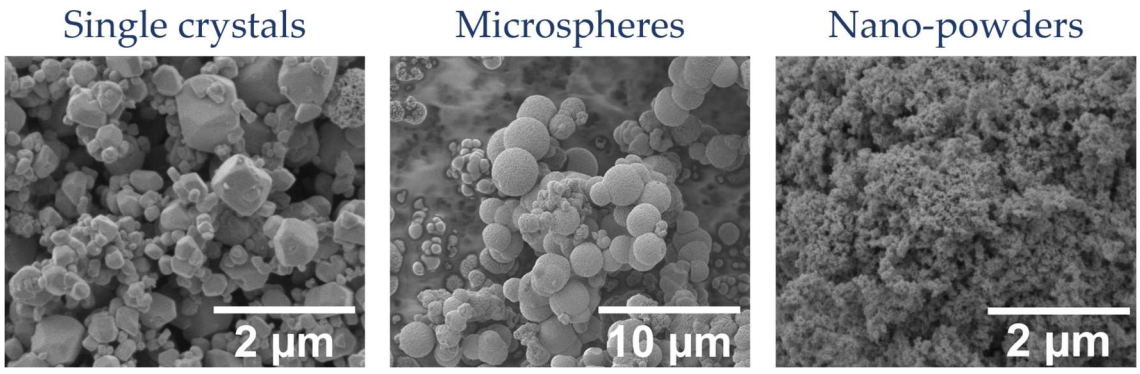

Figure 18. SEM images of three samples morphologies selected for the sintering study.

Moreover, preliminary dilatometric tests (not shown in this deliverable) revealed that a short heat treatment at 1600°C was not enough to fully densify the samples for samples prepared at pH = 1 (single crystals) and 2 (microspheres), and that higher temperature and/or longer heating times were required. Conversely, heating at 1600°C appeared to be sufficient or even too high to complete the densification for pellets made from the powder prepared at pH = 8 (nano-powders). Based on these differences, the study of the sintering of these three compounds was undertaken at three temperatures (1500°C, 1600°C and 1700°C) considering four heat durations (1h, 2h, 4h and 8h).

Density measurements

The geometric density of each pellet was measured after the various sintering conditions applied. In addition, density measurements by helium pycnometry were also carried out to discriminate open and closed porosities (**Table 10**). The geometric densities mostly confirmed the conclusions made from dilatometric study. Indeed, density values between 90 and 95% were obtained after 1 to 4 hours of heating at 1600°C for all the samples studied whatever the initial morphology of the powder. Moreover, these values revealed that sintering at 1500°C with a holding time of at least 4 hours appeared to be sufficient to obtain satisfactory densities, and even higher than the values obtained at 1600°C for nano-powders. In the case of single crystals and microspheres, these same conditions (*i.e.* 1500°C - 4h) allowed a significant reduction of the open porosity within the pellet (*i.e.* from more than 10% to 3%). For all the morphologies, the final stage of sintering, which corresponds to the elimination of closed porosities and is generally characterized by relative densities higher than 92%, seemed to be reached under these conditions (*i.e.* 1500°C - 4h).

Finally, it is worth noting that under certain sintering conditions, a loss of mechanical strength led to the total disintegration of the pellets. This phenomenon was observed for all morphologies after 8 hours of treatment at 1600°C and during several tests carried out at 1700°C as shown in **Table 10**. These results showed that high temperatures combined with excessive holding times led to stress within the pellets and to de-densification [59].

This project has received funding from the EURATOM research and training programme 2017-2021 under grant agreement No 755171

Table 10. Geometrical and pycnometric relative densities and associated values of porosities of the sintered samples prepared.

Morphology	Temperature (°C)	Heating time (h)	d_{geo} (%)	d_{pycno} (%)	Closed porosity (%)	Open porosity (%)
Single Crystals	1500	1	87	95	5	8
		2	87	98	2	11
		4	92	95	5	3
		8	94	97	3	3
	1600	1	95	99	1	4
		2	95	/	/	/
		4	94	98	2	4
		8	*break*	/	/	/
	1700	1	98	98	2	0
		2	*break*	/	/	/
		4	*break*	/	/	/
Microspheres	1500	1	86	97	3	11
		2	85	97	3	12
		4	91	94	6	3
		8	92	95	5	3
	1600	1	90	95	5	5
		2	94	/	/	/
		4	91	96	4	5
		8	*break*	/	/	/
	1700	1	96	97	3	1
		2	*break*	/	/	/
		4	96	97	3	1
Nano-powders	1500	1	94	98	2	4
		2	96	/	/	/
		4	96	99	1	3
		8	98	/	/	/
	1600	1	93	98	2	5
		2	93	/	/	/
		4	92	98	2	6
		8	*break*	/	/	/
	1700	1 - 4	*break*	/	/	/

Grains size distribution

In the absence of exaggerated growth phenomena, the grain size distribution in a sintered ceramic material is generally described through a log-normal model [60]. This is also the case whatever the sample considered in this study, as the logarithm of the frequency of grain size (**Figure 19**) systematically follows a Gaussian distribution. Therefore, all the results were expressed as the median grain size with the associated standard deviation.

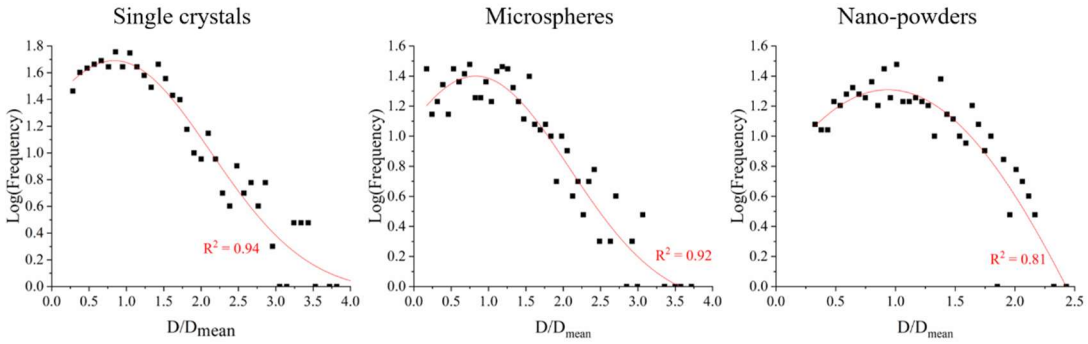

Figure 19. Representation of the logarithm of the frequency of the median grain size for the three morphologies considered after sintering at 1600°C for 1 hour. The red curve represents the Gaussian fit.

Typical variation of the microstructure of the pellets as a function of the sintering temperature (1 hour plateau) is illustrated in **Figure 20** for the three powders morphologies investigated. For single crystals and microspheres, the increase in grain size as well as the decrease in open porosity as a function of the increase in sintering temperature was clearly observed. Indeed, for both morphologies the median grain size increased from less than 1 µm after sintering at 1500°C to 5 µm at 1700°C with a grain size distribution ranging from 1 to 9 µm. In contrast, the median grain size did not change significantly as a function of the sintering temperature for nano-powders (*i.e.* 3-4 µm). The initial precipitation of nanosized powders was then still compatible with the pellet's microstructure characterized by micro-sized grains. This was explained by the higher reactivity of the nano-powders which led to faster grain growth kinetics. In addition, it is important to note the low inter-granular porosity of the pellets prepared from nano-powders at 1500°C and 1600°C compared to the other two morphologies.

Sintering map

The sintering map is a graphical representation of the variation of the mean (or median in our case) grain size as a function of the relative density of a sample [61, 62]. This tool is very interesting to highlight the impact of powder preparation conditions (*e.g.* temperature, synthesis time and pH) on sintering, and to monitor the microstructure of the final sample. Nevertheless, very few data were reported for actinide-based compounds, including oxides. For example, Clavier *et al.* produced a sintering map for ThO_2 by combining *in situ* grain size determination by High-Temperature Environmental Scanning Electron Microscopy (HT-ESEM) and density values extrapolated from dilatometric measurements [63]. More recently, sintering maps based on experimental data were also reported for other An-based oxides such as $Th_{1-x}Y_xO_{2-x/2}$ [64] and $(U,Pu)O_{2\pm x}$ [65].

Thus, the density and grain size values of the samples prepared in this work and reported in the previous sections were used to establish the three trajectories showing the impact of the powder morphology on the final microstructure of the pellets (**Figure 21**).

This project has received funding from the EURATOM research and training programme 2017-2021 under grant agreement No 755171

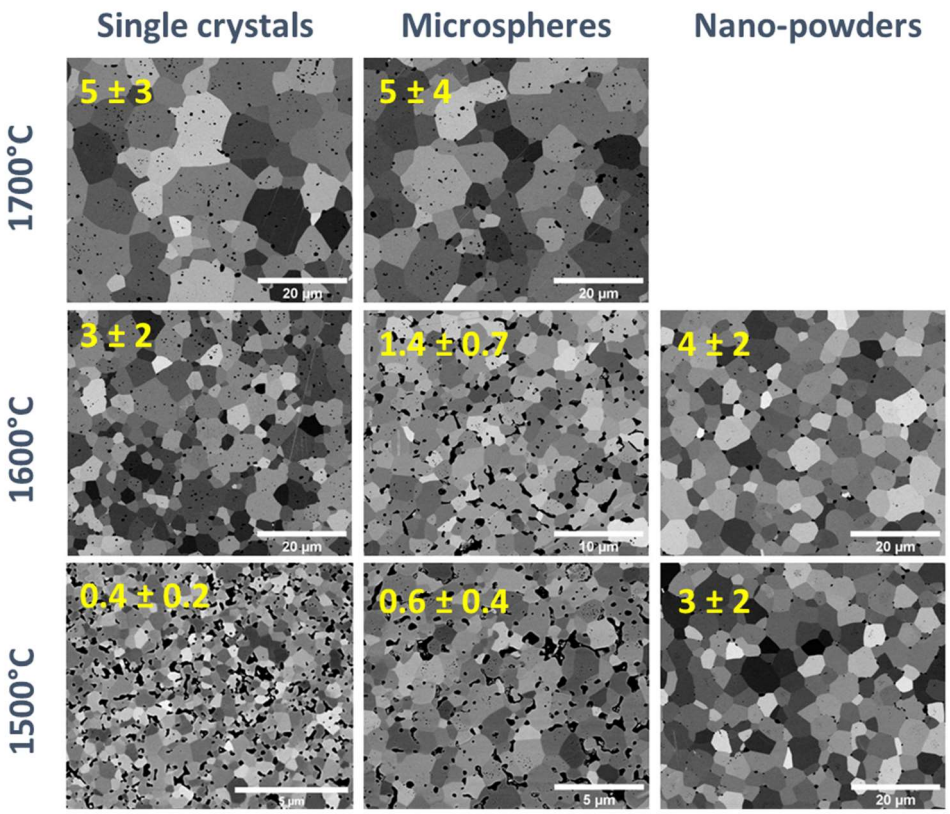

Figure 20. Evolution of the grain size as a function of the morphology of the initial powders and the sintering temperature for a holding time of 1 hour. The median grain size is indicated in yellow in the pictures and expressed in µm.

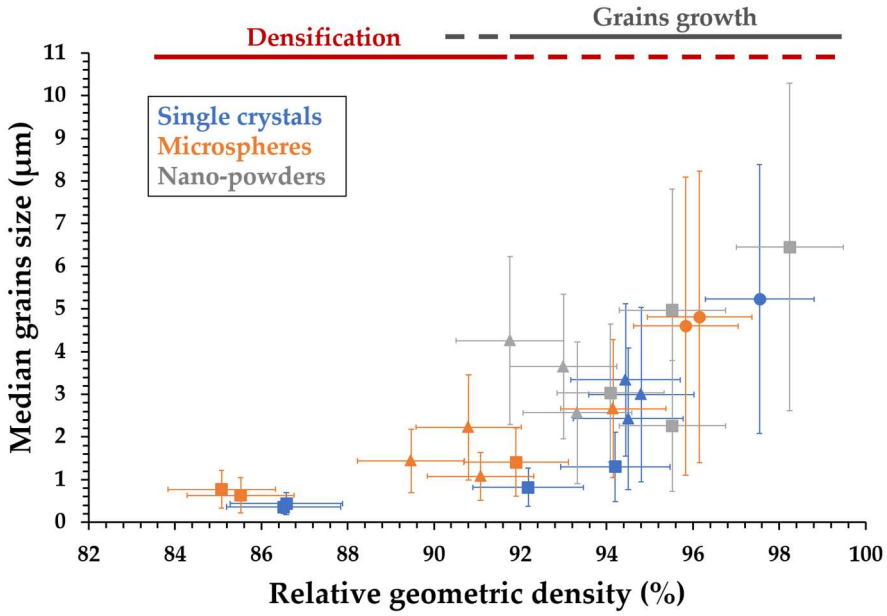

Figure 21. Sintering map of uranium oxides prepared by hydrothermal conversion of oxalate precursors. Single crystals, microspheres and nano-powders are represented in blue, orange and grey, respectively. Symbols account for the

three sintering temperatures investigated, 1500°C (squares); 1600°C (triangles) and 1700°C (circles).

The behaviour of single crystals and microspheres was in good agreement with the sintering trajectories generally observed in the literature[63, 64, 66-69]. Indeed, the development of the microstructure can be divided in two parts: the first one is mainly governed by the densification of the sample (from 85 to 92 %TD) and is accompanied by a limited grain growth. As such, it can be considered to account for the first and intermediate steps of the sintering process, which correspond successively to the elaboration of necks between grains and then to the elimination of open porosity. Subsequently, the second part is characterised by a significant increase in grain size (typically by a factor of 2 or 3) and is only accompanied by a slight densification (< 5%). The transition between these two regimes of microstructure development typically occurred for relative densities ranging between 91 and 95 %TD, which is in agreement with the empirical limit of 92 %TD reported by Bernache-Assolant *et al.*[70].

In contrast, the behaviour of nano-powders differed from the other two morphologies. As described above, only data obtained after heating at 1500°C and 1600°C were compiled to plot the sintering trajectory, the samples sintered at 1700°C being broken. In this case, it should be noted that the relative densities measured were systematically higher than 90% which led to observe only a grain growth step on the sintering map. Thus, the densification mainly occurred at lower temperature compared to the other two morphologies.

To our knowledge, such a low temperature of densification for uranium and/or thorium oxides was only reported up to now by using Spark Plasma Sintering (SPS) which is known to improve the sintering kinetics [40, 71, 72]. On this basis, nano-powders synthesised through hydrothermal conversion of uranium (IV) oxalate at pH = 8 clearly presented the best ability to sinter among the set of samples investigated. Their large specific surface area, which increased their reactivity, allowed to reduce the sintering temperature by at least 100°C (*i.e.* T ≤ 1600°C) compared to the current nuclear fuel fabrication processes [7,45] with densities close to 95%.

Sintering mechanisms

The evolution of the average grain size within a porous ceramic material can be described by the equation:

$$D^n - D_0^n = kt \quad \textbf{(4.)}$$

Where D (or D_0) is the median grain diameter at time t (or t = 0) and n is a whole number depending on the diffusion mechanism responsible for the grain growth. k is the rate constant and depends on temperature according to Arrhenius' law:

$$k = k_0\, e^{\left(\frac{-E_A}{RT}\right)} \quad \textbf{(5.)}$$

With R the universal constant of perfect gases, E_A the activation energy and T the temperature.

In our case, the use of submicrometric starting powders means that D_0 is much lower than D [73]. It is then possible to simplify the expression of grain growth as follows:

$$D^n = k_0\, e^{\left(\frac{-E_A}{RT}\right)} t \quad \textbf{(6.)}$$

This equation was established considering that the granulometric distribution within the sample remained similar whatever the sintering time. Based on this hypothesis, the normalized distribution should be invariant as a function of time [74]. This co-called self-similarity of the grain size distribution as a function of time was reported experimentally [64, 66, 75, 76] and by Monte Carlo calculations [77] for ceramic systems and resulted from the invariance of each grain class (*i.e.* constant D/D_{mean} ratio).

In this work, a systematic study of the cumulated grain size distribution was undertaken at different temperatures and systematically led to a sigmoidal trend whatever the starting powder considered. An example taken from the pellets prepared from nano-powders at 1500°C is presented in **Figure 22**. In addition, the standardised particle size distribution (D/D_{mean}) within the samples appeared almost identical whatever the sintering time: the grain growth process was therefore considered as normal. This meant that no exaggerated growth, leading to the detachment of intergranular pores and grain boundaries, took place during the sintering process.

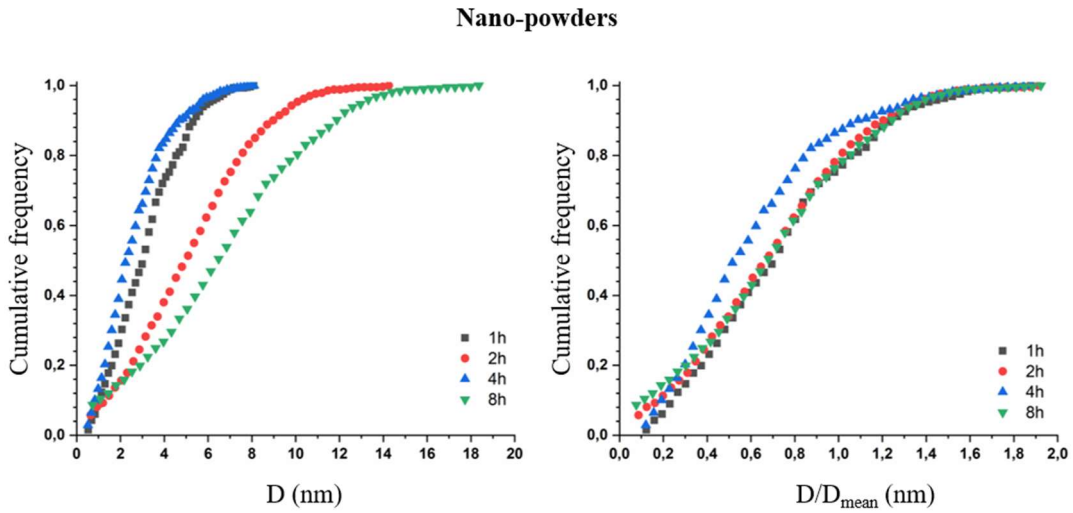

Figure 22. Representation of the particle size distribution within the pellets obtained from nano-powders at 1500°C.

For all the samples studied, the grain size distribution being normal, the value of the exponent n, characteristic of the grain growth mechanism, was extracted from the equation:

$$n \ln(D) = \ln(t) - \frac{E_A}{RT} + \ln(k_0) \qquad \textbf{(7.)}$$

For the three morphologies studied and the set of sintering conditions tested, the variation of ln(D) as a function of ln(t) is given in **Figure 23**. The small number of experimental data points considered for each temperature, as well as the wide particle size distribution observed in the samples, did not allow to systematically conclude unambiguously to a linear variation. The value of n was therefore estimated at 1500°C for the three morphologies and at 1600°C for single crystals only.

This project has received funding from the EURATOM research and training programme 2017-2021 under grant agreement No 755171

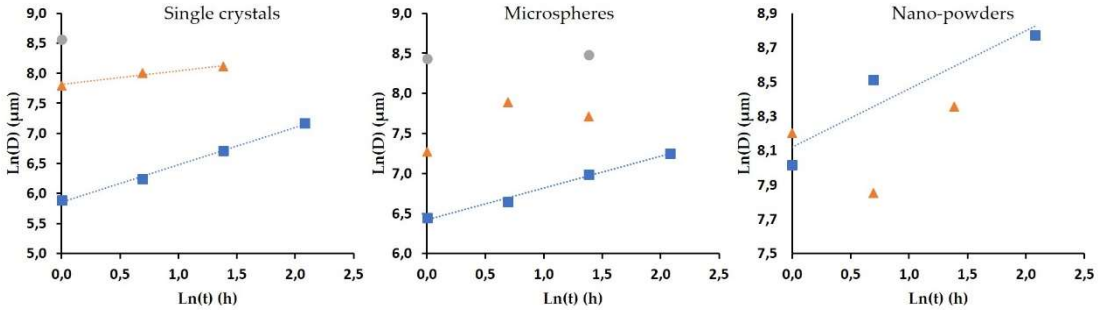

Figure 23. Variation of ln(D) as a function of ln(t) during sintering of the powders with different morphologies at 1500°C: ■ ; 1600°C: ▲ ; 1700°C: ● .

For single crystals and microspheres, the n value was close to 2 at 1500°C compared to 3 for nano-powders. Based on the high uncertainty for the determination of the n value for nano-powders, we considered that the three morphologies exhibited the same value close to 2. In the case of a material with impurities, this corresponds to a granular growth controlled by the movement of the grain boundaries but slowed down by the presence of impurities at the grain joints (the "solute drag" phenomenon). This result was consistent with the observation of residual carbon trapped between the crystallites. Indeed, in our previous work[78] on ThO_2 samples prepared by the same hydrothermal process than that described in this paper, EXAFS experiments allowed to exclude the presence of residual carbon trapped inside the unit cell and rather accounted for the existence of amorphous carbon between the crystallites. Such impurities would finally slow down the motion of grain boundaries during the sintering process by limiting the diffusion of uranium. In case of single crystals, which were found to be almost carbon-free (*cf.* **Table 9**), the presence of numerous intragranular pores, as shown in **Figure 20** could lead to the same phenomena, i.e. decrease of the grain boundaries motion [70].

In the case of sintering of single crystals, however, the n value estimated at 1600°C was close to 4. This indicated that the movement of the grain boundaries was then controlled by diffusion at the grain boundaries, and that the braking phenomenon described above disappeared at this temperature. The increase in sintering temperature could therefore have allowed a fraction of the residual carbon to be removed. Moreover, this result was in agreement with the observations of Nkou Bouala *et al.* on the sintering of ThO_2 between 1000 and 1300°C whose diffusion took place preferentially at the grain boundaries [79].

Subsequently, the activation energy related to grain growth during the sintering of UO_{2+x} was determined from equation (7.) for the three morphologies studied. Although numerous studies were dedicated to the determination of activation energies since the 1960's, the range of values reported in the literature remained very scattered. Also, due to the wide domain of temperatures investigated by the authors, these data probably encompassed phenomena related to the first step of sintering (i.e. elaboration of necks between the grains) with the grain growth. A common trend was still described, with the highest values of E_A attached to stoichiometric $UO_{2.00}$, typically around 390-400 $kJ.mol^{-1}$. The activation energy then decreased when the oxide became slightly hyper-stoichiometric, down to around 220 $kJ.mol^{-1}$ for $2.002 < O/U < 2.1$ [80, 81]. Above this value, E_A increased again in the upper range of the UO_{2+x} stoichiometry (i.e. typically $x > 0.15$), mostly due to the formation of complex defects in the crystal lattice and/or due to the formation of UO_{2+x}/U_4O_9 mixtures.

Table 11. Activation energies associated with granular growth during sintering of the three UO_{2+x} morphologies studied, and comparison with the literature.

Sample	E_A (kJ/mol)	Reference
$UO_{2.00}$	390 – 400	82-84
$UO_{2.002-2.10}$	220 – 230	2
$UO_{2.10-2.20}$	300 – 400	83-86
Single crystals	422 ± 50	
Microspheres	283 ± 63	This work
Nano-powders	113 ± 62	

In good agreement with these data, the values determined during this study differed significantly depending on the hydrothermal conversion conditions, as a result of the subsequent changes in both morphology and stoichiometry of the powders (**Table 11**). As such, the activation energy reached 422 ± 50 kJ/mol for single crystals, which corresponded to the upper range of values reported for UO_2 [82-84]. Such a high value was ascribed to the low reactivity of the powder (lowest value of specific surface area in the set of samples investigated) and to the O/U ratio which was close to 2 (**Table 9**). When both S_{Sa} and O/M increased, the activation energy measured decreased to reach the lower range of the reported values for UO_{2+x} [83-86], with E_A = 283 ± 63 kJ/mol for microspheres.

Furthermore, the activation energy determined during the sintering of the nano-powders was much lower than the values usually reported in the literature for UO_{2+x} (113 ± 62 kJ/mol). This variation related to the morphology was consistent with the literature describing the phenomena of granular growth in nanometric materials [87, 88]. Indeed, Shukla *et al.* showed that the activation energy of granular growth of a nanoscale yttrium-doped zirconia powder was much lower than that of the bulk material (*i.e.* 13 kJ/mol compared to 580 kJ/mol) [87]. In our case, the range of variation of the activation energy was not as huge but confirmed the very high sinterability of the nanometric powder prepared at pH = 8.

Conclusion

The sintering of uranium oxide powders prepared by hydrothermal conversion of the oxalate precursor was studied. Three samples with varied morphologies (single crystals - pH = 1, microspheres - pH = 2 and nano-powders - pH = 8) were thus selected to examine their sintering behaviour more precisely. Densitometric and granulometric data allowed to establish a sintering map for each of the powders considered. The study of the densification revealed that after a 4-hours heat treatment at 1500°C, all the powders exhibited relative densities above 90%TD. In the case of single crystals and microspheres, densities greater than or equal to 96% were also obtained at 1700°C. In contrast, a sintering time of only 2 to 8 hours at 1500°C led to comparable results for nano-powders prepared at pH = 8, due to their higher reactivity. The study of the grains size confirmed the difference between the behaviour of single crystals and microspheres, on the one hand, and nano-powders, on the other hand. For the first two powders, the grains size increased with temperature and sintering time, whereas this growth remained very limited for nano-powders, making it possible to manufacture dense nanostructured samples.

This project has received funding from the EURATOM research and training programme 2017-2021 under grant agreement No 755171

The study of sintering mechanisms finally revealed a behaviour consistent with the presence of insoluble impurities (carbon) or porosity in the uranium oxide pellet. The determination of the activation energy associated to the grain growth showed a strong decrease in the latter with the decrease in size of the objects studied, from 420 ± 50 kJ/mol for single crystals to 110 ± 60 kJ/mol for nano-powders. Thus, the results obtained from the nano-powders prepared at pH = 8 under hydrothermal conditions seemed to be the most promising, with a sintering temperature to reach a density of 96%, 200°C lower than that found for the other morphologies or that used for the manufacture of nuclear fuel in France (*i.e.* 1700°C).

These observations therefore confirmed that the hydrothermal conversion of oxalates is a promising route for the synthesis of actinide oxides, which can be subsequently sintered without any preliminary treatment. In terms of process, this allows the reduction of the number of steps by comparison to the thermal conversion conventionally carried out after oxalate precipitation.

This project has received funding from the EURATOM research and training programme 2017-2021 under grant agreement No 755171

Numerous studies addressed the sintering of UO_{2+x} samples [80, 83, 89, 90] but mainly focused on intermediate and final stages, which are characterized by grain growth and pores elimination. Conversely, the first stage of sintering, associated with the formation of necks between the grains, was generally investigated through numerical simulations, using either molecular dynamics [91], Monte Carlo [92] or Discrete Elements methods [93]. Within all of these methods, approximations are made both on the morphology of grains (supposed to be perfect spheres) and on their crystalline state (single crystal). Then, the results obtained can be hardly used to provide a predictive and reliable description of the first stage of the sintering process, which is required to optimize the elaboration of nuclear fuels. In parallel, only few experimental works were dedicated to the first stage of UO_{2+x} sintering [82, 94, 95]. Moreover, the range of temperatures used in these studies, notably during dilatometry experiments, might have led the authors to encompass several phenomena, such as neck formation and densification/grain growth. Also, the exact stoichiometry of the samples frequently lacked of an accurate characterization.

This last point is particularly sensitive for uranium oxides. Indeed, uranium can adopt multiple oxidation states (mainly +IV, +V and +VI) that strongly modify the diffusion coefficients and then the sintering kinetics. As such, slightly hyper-stoichiometric oxides UO_{2+x} (with typically $x < 0.1$) are generally reported to sinter at lower temperature than stoichiometric $UO_{2.00}$ samples [83, 96-98]. Conversely, higher values of the O/U ratio, which can result in the formation of UO_{2+x}-U_4O_9 mixtures, are generally associated to an increase in the activation energy attached to the sintering process [83]. Nevertheless, the modification of the kinetics with the atmosphere used, hence with the O/U ratio in the sample, received different explanations in the literature, based either on the variation of the diffusion coefficient of uranium or on different diffusion mechanisms.

In order to address these different issues, and taking benefit from the preparation of size-controlled UOx microspheres through the hydrothermal conversion of Uranium (IV) aspartate, we undertook for the first time *in situ* High-Temperature Environmental Scanning Electron Microscopy (HT-ESEM) observations of the first stage of sintering of uranium oxide. These samples were selected as model compounds for real UO_{2+x} powders used in the fabrication of nuclear fuel as well as for the systems generally used in numerical simulations, composed of two spheres in contact. This approach, which allowed the determination of quantitative geometrical data describing the formation then the growth of a neck between spherical particles was already developed and tested on model compounds free from redox reactions [79, 99]. In the case of the present study, this methodology was adapted to various atmospheres in order to stabilize different uranium oxide-based phases. The accurate characterization of their stoichiometry in terms of O/U ratio and the associated morphological modifications observed during heat treatments at high temperatures (typically in the 900-1200°C range) will be reported herein. Then, the collected data will be used to evaluate the activation energy associated to the first step of the sintering, and to point out the driving diffusion mechanism.

General evolution of the sample's morphology

Series of HT-ESEM images recorded *in situ* at 1000°C under the various atmospheres investigated are gathered in **Figure 24**, and provide an example of the general evolution of the sample's morphology during the heat treatment.

This project has received funding from the EURATOM research and training programme 2017-2021 under grant agreement No 755171

For the lowest dioxygen partial pressure considered (i.e. $P_{O_2} = 10^{-10}$ Pa), which led to stabilize the nearly-stoichiometric $UO_{2.01}$, the formation and the continuous growth of a neck between the two spherical grains was clearly observed. It was accompanied by the increase of the crystallites size forming the particles, which was particularly obvious when comparing the micrographs collected after 6 and 18 minutes of heat treatment. Similar features were reported when working with $P_{O_2} = 10^{-1}$ Pa, however with different kinetics. Indeed, the size of the neck increased very quickly then reached a steady-state after only 15 minutes of heat treatment at 1000°C. Simultaneously, the average crystallite size also increased up to 100 nm, which appeared in good agreement with the data obtained from PXRD analysis.

Beyond their inner microstructure, the particles were found to undergo important morphological modifications when working in air (P_{O_2} = 25 Pa). During the heat treatment, the general shape evolved from spherical to ovoid, which was probably linked to the transformation of UO_{2+x} into U_3O_8. Indeed, this oxidation reaction was accompanied by a 37% increase of the unit cell volumes when turning from U_3O_{8-x} (with x = 1) [100] to U_3O_8. While the associated constraints can generate abundant cracking in the nuclear fuel pellets [101], there are more likely to be accommodated through deformation in the case of our sub-micrometric particles. This deformation then occurred simultaneously to the growth of the crystallites, almost immediately after injecting the gas in the HT-ESEM chamber. From the image series reported in **Figure 24**, crystallites also reached their maximum size only few seconds after the onset of the isothermal dwell. Similarly, the growth of the neck between the particles was accelerated and reached a steady-state after only 7 minutes of heat treatment.

This project has received funding from the EURATOM research and training programme 2017-2021 under grant agreement No 755171

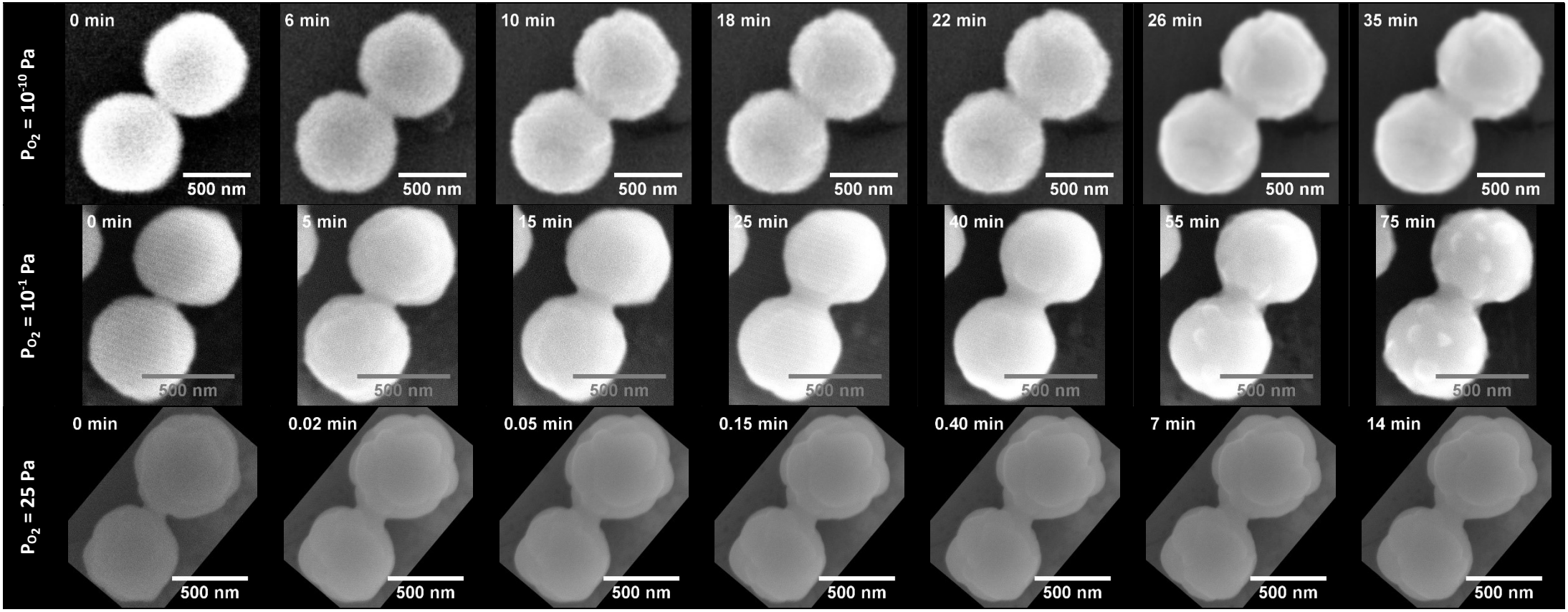

Figure 24. HT-ESEM images recorded *in situ* during heat treatment at 1000°C of uranium oxide microspheres under various atmospheres.

This project has received funding from the EURATOM research and training programme 2017-2021 under grant agreement No 755171

Kinetics of sintering first step

From the data reported in the previous section, the neck formation and crystallites growth occurred systematically in the systems investigated, although with different kinetics. As such, the quantitative evaluation of geometrical parameters of interest was used to monitor the first step of sintering. Particularly, the diameter of the neck (x) and the average diameter of the particles (r) were measured, as well as the distance between the sphere centres (d). Using this data, it was possible to calculate and plot the evolution of the dimensionless parameter λ, called sintering degree, and generally used to describe the first stage of sintering at the grain scale:

$$\lambda = x/r \qquad \textbf{(8.)}$$

Figure 25 reports the evolution of both x, r, d and λ parameters during the heat treatment of the particles at 830°C in air (P_{O_2} = 25 Pa). In this example, which reflected most of the data collected, the diameter of the spherical particles used during the study remained mostly unchanged. Indeed, only a 3% diameter decrease was stated, which was ascribed to the volatilization of residual water and organics trapped in the microstructure, as well as to the elimination of inner porosity initially present in the particles. Simultaneously, the distance between the centres of the particles decreased by around 5%, thus attesting that densification of the system already started. Finally, the growth of the neck between the grains was observed during the first 60 minutes of the heat treatment, then reached a steady-state. As the variation of the grain size could be considered as negligible, the variation of the λ parameter followed the same trend, and reached a steady state after around 60 minutes of heating.

In order to directly visualize the effect of the atmosphere on the sintering kinetics, the evolution of the λ parameter at 1000°C was plotted in **Figure 26** for the three values of P_{O_2}. As already stated, the general behaviour observed was similar in all the cases, with the variation controlled by the growth of the neck between the two spherical particles, the diameter of these latter being mostly unchanged. Nevertheless, the kinetics appeared to be strongly modified by the dioxygen partial pressure. In this example, an equilibrium state was reached in less than 10 minutes in air (P_{O_2} = 25 Pa). Conversely, the process slowed down when P_{O_2} decreased (i.e. $P_{O_2} = 10^{-1}$ Pa) while no steady-state was observed after 2 hours of heating treatment with $P_{O_2} = 10^{-10}$ Pa.

This project has received funding from the EURATOM research and training programme 2017-2021 under grant agreement No 755171

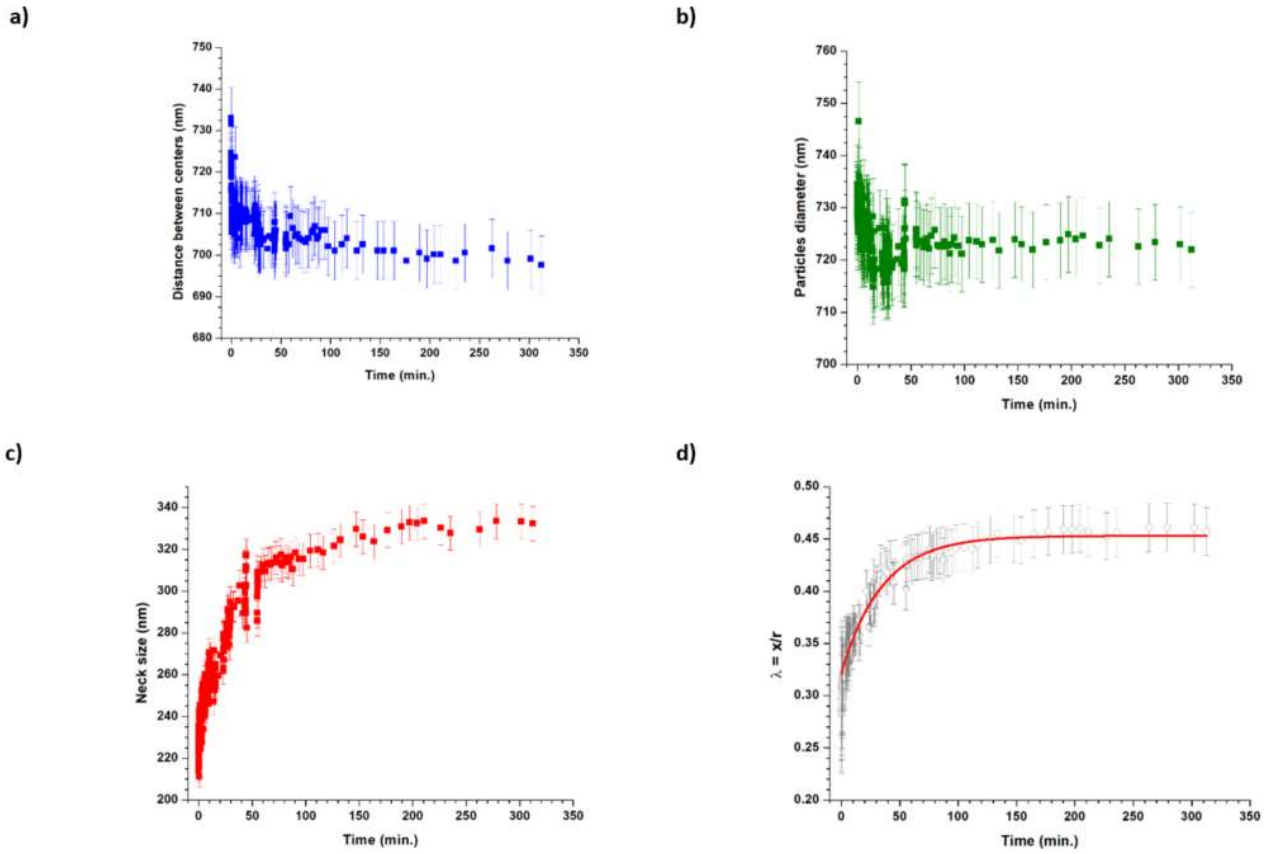

Figure 25. Evolution of the distance between the grains centres, d, (a); average grain diameter, r (b); neck diameter, x, (c); and dimensionless parameter, λ, (d) during heat treatment of the 700 nm-diameter particles at 830°C under air (P_{O_2} = 25 Pa).

This project has received funding from the EURATOM research and training programme 2017-2021 under grant agreement No 755171

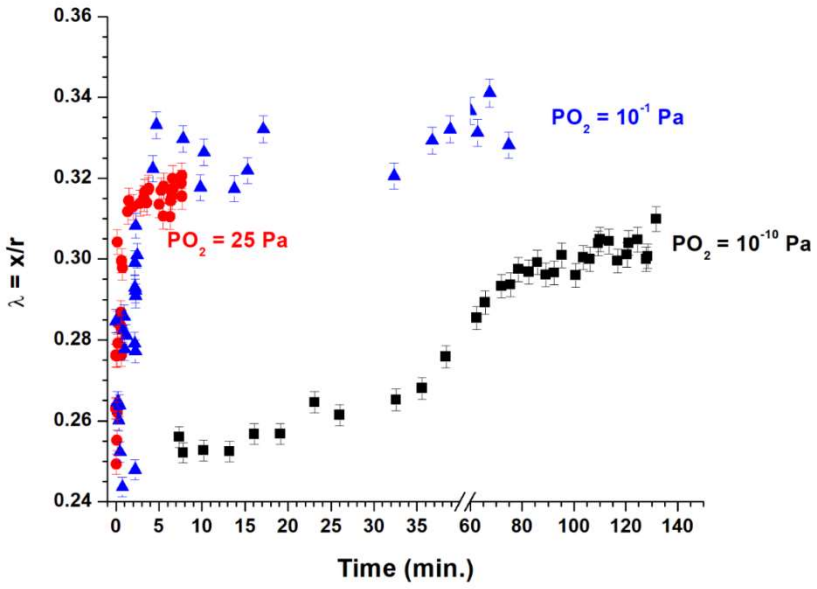

Figure 26. Evolution of the dimensionless parameter λ = x/r obtained at 1000°C for P_{O_2} = 10^{-10} Pa (■); 10^{-1} Pa (▲) and 25 Pa (●).

The kinetic constants associated to the elaboration of the neck during the first step of the sintering were then determined by fitting the experimental data. From a mathematical point of view, our datasets were fitted either with an exponential or a power law. Both kinds of models led to satisfactory correlation factors (i.e. typically around 0.9), which quality was mainly impacted by the scattering of the experimental data. From the physico-chemical point of view, the general model of neck growth developed during the 1950's [102], was based on a power law such as:

$$\lambda^n = \frac{k.t}{r^m} \quad \textbf{(9.)}$$

where λ = x/r is the dimensionless parameter describing the sintering degree, k is a kinetic constant, t is the duration of heat treatment, and *n* and *m* are exponents characteristic of the diffusion process involved (i.e. mainly surface, volume or grain boundary diffusion).

Nevertheless, this model was based on the hypothesis of single-crystal grains, which was not the case in this study, as the spherical particles used herein were clearly shown to be polycrystalline. As the evolution of λ cannot be described by usual sintering models in the case of polycrystalline particles, we used a first-order kinetic law to fit the datasets obtained through HT-ESEM observations the evolution of the system, with:

$$\lambda = [a]_0 \times \exp^{-kt} + \lambda_0 \quad \textbf{(10.)}$$

This project has received funding from the EURATOM research and training programme 2017-2021 under grant agreement No 755171

where $[a]_0$ is a pre-exponential factor, λ_0 the sintering degree at t = 0, and k the kinetic constant (expressed in s^{-1}).

This approach was already used successfully during the study of early stages of CeO_2 and ThO_2 [79, 99], and again led herein to good correlation factors (typically ≥ 0.9) for all the experimental conditions investigated, as evidenced in **Figure 25d**. It was then possible to assess the value of the kinetic constant associated to the elaboration of the neck between the two spherical particles for all the operating conditions considered in terms of temperature and P_{O_2} (**Table 12**).

Table 12. Summary of the kinetic constants associated to neck elaboration determined for various operating conditions.

$P_{O_2} = 10^{-10}$ Pa		$P_{O_2} = 10^{-1}$ Pa		$P_{O_2} = 25$ Pa	
T (°C)	**k (s^{-1})**	**T (°C)**	**k (s^{-1})**	**T (°C)**	**k (s^{-1})**
885	0.025 ± 0.004	925	0.0080 ± 0.0005	830	0.028 ± 0.006
900	0.03 ± 0.01	950	0.104 ± 0.001	870	0.08 ± 0.01
920	0.033 ± 0.003	965	0.028 ± 0.005	910	0.092 ± 0.005
950	0.035 ± 0.003	980	0.039 ± 0.007	930	0.114 ± 0.005
965	0.060 ± 0.002	1000	0.11 ± 0.03	950	0.35 ± 0.02
1010	0.157 ± 0.002	1050	0.19 ± 0.02	980	0.70 ± 0.04
1050	0.388 ± 0.001			1000	1.5 ± 0.1

Determination of the activation energy

The kinetic constant determined for all the conditions considered in terms of temperature and atmosphere were further plotted in an Arrhenius diagram (**Figure 27**). For the three values of P_{O_2} investigated, the variation of ln(k) versus the reciprocal temperature followed a linear trend, showing that the first step of sintering was driven by a unique diffusion mechanism for the interval of temperatures considered (typically 800-1100°C). This observation then contradicted the results reported by Lahiri *et al.* who pointed out the modification of the diffusion mechanism operating during the sintering of stoichiometric $UO_{2.00}$ at around 1050°C [90].

This project has received funding from the EURATOM research and training programme 2017-2021 under grant agreement No 755171

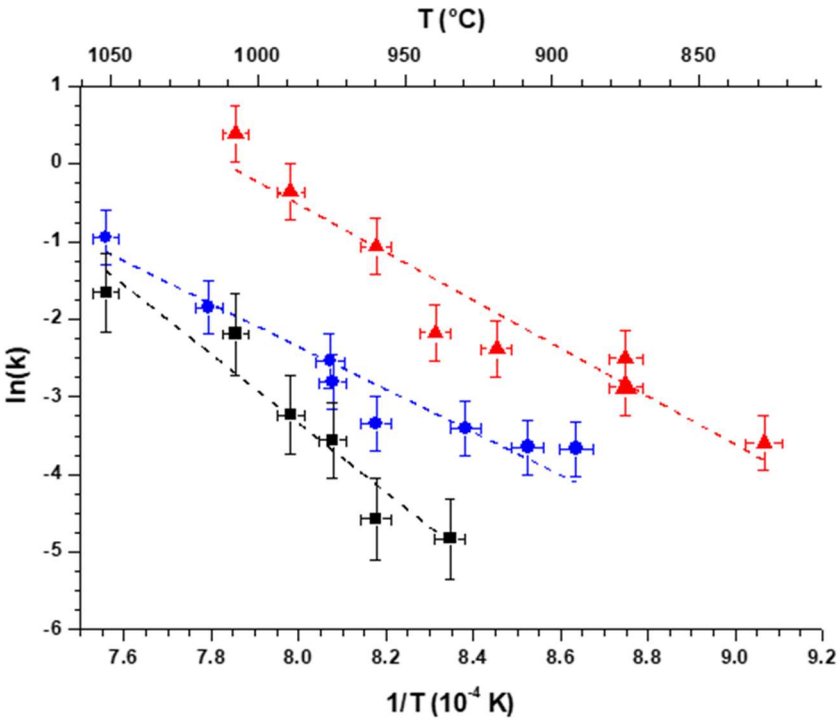

Figure 27. Variation of ln(k) versus the reciprocal temperature associated to the first step of sintering of uranium oxides for various dioxygen partial pressures : P_{O_2} = 10^{-10} Pa (■); P_{O_2} = 10^{-1} Pa (●) and P_{O_2} = 25 Pa (▲).

The activation energies calculated from the variation of the kinetic constant for the three atmospheres investigated are gathered in **Table 13**. Several authors already reported E_A values attached to the first step of the sintering of uranium dioxides. They systematically used bulky samples (i.e. pellets) and mostly based their works on dilatometry measurements through different methods such as Dorn's or Constant Heating Rate (CHR). The first studies undertaken in the 1960's led to extremely scattered results, with values ranging from 80 to 460 kJ.mol^{-1} [103,104]. Improving the control on the samples stoichiometry further led to more accurate measurements and allowed to reach a consensus on several points. First, the activation energy attached to the first step of sintering for a stoichiometric $UO_{2.00}$ was generally reported around 390-400 kJ.mol^{-1} [82], while it decreased when the oxide becomes hyper-stoichiometric, with values typically around 220 kJ.mol^{-1} for 2.002 < O/U < 2.1 [80, 81]. Nevertheless, some uncertainties still persisted in the accurate determination of the O/U ratio in these samples. Also, the temperature ranges studied were wide, which could have led to encompass both neck elaboration and densification/grain growth phenomena. As such, Ainscough *et al.* showed that an activation energy of 260 kJ.mol^{-1}, very close to those cited above, was obtained when studying grain growth in a $UO_{2.00}$ pellet between 1300 and 1500°C [105]. Actually, the activation energy only differed significantly when reaching very high temperatures, where the processes observed became easily discernible from the first step of

This project has received funding from the EURATOM research and training programme 2017-2021 under grant agreement No 755171

sintering. As a matter of example, Singh concluded to a value close to 500 kJ.mol^{-1} between 1800 and 2100°C [106].

In order to overcome all these discrepancies, more recent works reinvestigated critically the first step of UO_{2+x} sintering, with the aim to specify the driving mechanism and associated activation energies. The values gathered in the review by Knorr *et al.* [98], as well as those determined by Dehaudt *et al.* through different methods [83], seemed to be the most accurate available up to date, and will be used as reference values. Also, these authors explored the upper range of the UO_{2+x} stoichiometry (i.e. typically x > 0.15), which was previously poorly documented.

Table 13. Activation energies associated to the first step of sintering for various uranium oxides stabilized in our operating conditions.

P_{O_2} (Pa)	Atmosphere	Oxide	Activation energy (kJ.mol^{-1})
25	120 Pa Air	U_3O_8	260 ± 40
10^{-1}	100 Pa N_2 / 1000 ppm O_2	$UO_{2.21}$	370 ± 50
10^{-10}	150 Pa N_2 / 5% H_2 / 0,2% ppm H_2O	$UO_{2.01}$	210 ± 25

The activation energies calculated in this study were generally found to be in very good agreement with the reference data selected in the literature. A very small hyper-stoichiometry (x = 0.01) was associated to the lowest value of E_A, close to 200 kJ.mol^{-1}. Conversely, regarding to highly hyper-stoichiometric UO_{2+x}, the value determined for $UO_{2.21}$ was found between those published for $UO_{2.17}$ and $UO_{2.22}$ by Dehaudt *et al.* (323 and 437 kJ.mol^{-1}, respectively) [83]. Nevertheless, it did not comply with the hypothesis of a threshold between these compositions linked with the structural transition from UO_{2+x} to U_4O_{9-y}, and to the subsequent modification of uranium diffusion coefficient. Finally, to the best of our knowledge, the value determined for the first step of U_3O_8 sintering (260 kJ.mol^{-1}) was the first to be published. It was close to that generally reported for uranium dioxides exhibiting O/U ratios close to 2, and then appeared to be significantly lower than those of $UO_{2.00}$ and U_4O_9. This result then backed up the use of U_3O_8 as a sintering aid during the fabrication process of UOx or MOx fuels, particularly when recycling scraps [107, 108].

Also, it is important to underline that the values obtained in this study could be considered as references for further works. First, the characterization technique used for the determination of the data allowed us to unambiguously discriminate the first step of sintering, as only geometrical measurements coming from neck elaboration were considered. Also, the stoichiometry of the samples was fixed through the monitoring of the surrounding atmosphere in the HT-ESEM chamber, then checked by both theoretical and experimental means. Moreover, the sub-micrometric size of our sample led us to prevent any stoichiometry gradient effect in the solid phase, which could not have been excluded when working with bulk samples, especially when preparing the materials through powder metallurgy processes.

This project has received funding from the EURATOM research and training programme 2017-2021 under grant agreement No 755171

Diffusion mechanism

The sintering of ceramics can be driven by different diffusion processes, i.e. surface diffusion, volume diffusion, grain boundary diffusion, evaporation-condensation and viscous flow. Only three of these mass transport mechanisms take part in the densification of the sample: grain boundary diffusion, volume diffusion and, in the case of liquid phase sintering, viscous flow. In our study, this densification was evidenced by the decrease of the distance between the centres of the two spherical particles of uranium oxides (**Figure 25a**).

The prevailing diffusion mechanism driving the sintering of a ceramic material was generally evidenced by determining the values of the *m* and *n* exponents involved in the general kinetic law used to describe the neck elaboration (equation 9). However, as stated before, this equation cannot be applied to our polycrystalline particles. For such systems, we therefore used the Herring's scaling law, which expresses the influence of particles size on the microstructural modifications of the sample during sintering. For grains presenting similar shapes, although with different sizes, sintered in identical experimental conditions, the Herring's scaling law predicts the relative time required to reach a given sintering degree (i.e. same λ value) [109]. When considering two spherical grains in contact with different radii, the following expression can be established [110] :

$$\frac{t_1}{t_2} = \left(\frac{r_1}{r_2}\right)^m \qquad \textbf{(11.)}$$

Where r_1 and r_2 are the grains radii, t_1 and t_2 the sintering times, and *m* an exponent specific to the diffusion mechanism operating during sintering, with *m* = 1 for viscous flow; *m* = 2 for evaporation-condensation; *m* = 3 for volume diffusion and *m* = 4 for surface diffusion or grain boundary diffusion.

Different experiments were then undertaken, starting with uranium oxide microspheres presenting diameters of 700 and 1400 nm. The comparison of the results obtained for the two systems during a heating treatment at 930°C under air (P_{O_2} = 25 Pa) is provided in **Figure 28** as an example. As expected from the general kinetic laws of sintering, which are systematically proportional to (1/r), the two-grains system composed of the smallest particles evolved more rapidly. Two values of λ reached by the two systems were then selected arbitrarily and the associated times were determined. These data, gathered in **Table 14**, allowed us to determine *m* values close to 3, which accounted for volume diffusion.

More importantly, similar results were obtained whatever the atmosphere considered, and thus whatever the dioxygen partial pressure. Hence, in the range of temperatures considered, the mechanism driving the first step of sintering was not significantly modified by the experimental conditions. It remained controlled by volume diffusion. This result contradicted previous reports attesting of the prevalence of grain boundary diffusion during the sintering of UO_{2+x} [80]. Nevertheless, it is worth noting that all these studies were based on the use of bulk samples, which could have led to convolute different phenomena occurring during the heating treatment of the ceramic material, particularly neck formation and grain growth. Nevertheless, such a discrepancy was not mentioned in our previous works, where HT-ESEM studies of CeO_2 and

This project has received funding from the EURATOM research and training programme 2017-2021 under grant agreement No 755171

ThO_2 both concluded to grain boundary diffusion as the driving mechanism of the first step of sintering [79, 99].

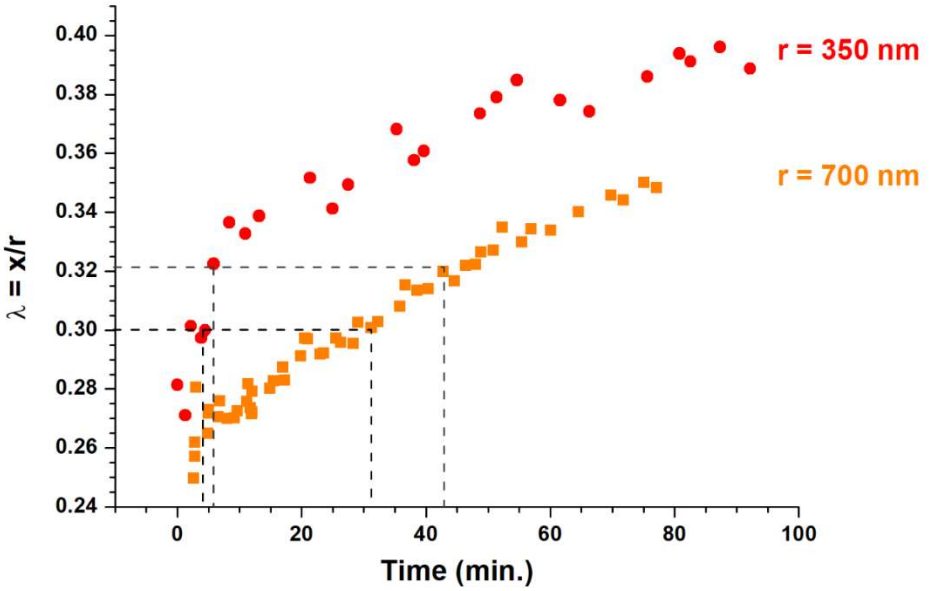

Figure 28. Comparison of the evolution of the λ parameter at T = 930°C and P_{O_2} = 25 Pa for systems composed of spherical particles of 700 nm (●) and 1400 nm (■) in diameter.

Table 14. Summary of the values obtained for the determination of the prevailing mechanism operating during the first step of uranium oxide sintering in the different atmospheres investigated.

x/r	t_1 - 700 nm (min.)	t_2 - 1400 nm (min.)	m
1010°C – P_{O_2} = 10^{-10} Pa			
0.208	3.05	21.75	2.83
0.203	2.65	26.42	3.32
1050°C – P_{O_2} = 10^{-1} Pa			
0.3	5.93	50.48	3.09
0.285	4.48	36.53	3.03
930 °C – P_{O_2} = 25 Pa			
0.32	5.85	48.05	3.04
0.3	3.83	25.57	2.74

This project has received funding from the EURATOM research and training programme 2017-2021 under grant agreement No 755171

On this basis, it is important to remember that several diffusion mechanisms always operate simultaneously during the sintering of ceramic or metallic materials. In the case of uranium oxides, it is then likely that volume and grain boundary diffusion present comparable contributions to the global kinetics. The modification of experimental parameters, such as the temperature, the atmosphere, or the grain size, could then generate inversion in the prevailing diffusion path. As such, the use of sub-micrometric particles in our study could be considered as one important explanation to the differences observed with other works employing bulk materials composed of micrometric grains. In these conditions, it is crucial to consider all the diffusive processes possible when modelling the first step of sintering. This is particularly the case for UO_{2+x}, for which the models frequently consider surface and grain boundary diffusion but neglect volume diffusion [111].

Conclusion

The first step of the sintering of various uranium oxides was monitored *in situ* for the first time through HT-ESEM observations, allowing to evidence directly the impact of the dioxygen partial pressure over the kinetics of neck elaboration. In all the operating conditions tested, image processing led to the determination of quantitative data describing the evolution of two-grain systems morphology. Although the growth of the nanometric crystallites composing the spherical grains was not followed in this study, the formation and the development of a neck between the particles was clearly evidenced. It was not accompanied by a significant decrease of the grains diameter, even if deformation was noted under the most oxidative atmosphere studied.

As the polycrystalline systems studied herein did not comply with the general kinetic laws of sintering, the evolution of the λ dimensionless parameter describing the sintering advancement was fitted using a simple first-order law. It first allowed us to evaluate the activation energy attached to the first step of sintering in the different conditions tested. When the dioxygen partial pressure led to stabilize hyper-stoichiometric UO_{2+x} oxides, the values obtained were found to increase with x, typically in the 200-400 $kJ.mol^{-1}$ range. Also, since the experimental technique used in this study strictly addressed the first step of sintering, i.e. formation of a neck between the particles, these values led to clear up the scattered data present in the literature and comforted some of the most recent studies. Under air atmosphere, the stabilization of U_3O_8 allowed us to provide the first evaluation of activation energy for the first step of sintering. This latter was close to that obtained for UO_{2+x} for low values of x, and was thus significantly lower than that obtained for stoichiometric $UO_{2.00}$ and U_4O_9. This result then supported the use of U_3O_8 as an aid for the sintering of oxide nuclear fuel pellets, especially when recycling scraps. According to the Herring scaling law, the main diffusion mechanism driving the first step of sintering was volume diffusion, independently from the stoichiometry of the uranium oxide. This work then provided an original set of data that can be implemented in numerical models describing the sintering of UO_{2+x}.

This project has received funding from the EURATOM research and training programme 2017-2021 under grant agreement No 755171

GENERAL CONCLUSIONS

Within the development of new generations of reactors, wet chemistry routes are studied for the fabrication of mixed oxide fuels such as $(U,Pu)O_2$ MOx, notably to improve the cations distribution homogeneity. In this framework, our work aimed at directly synthesizing uranium-based oxide samples from solution using hydrothermal conditions, and evaluate their sintering ability.

Samples were first prepared through the hydrothermal conversion of oxalate precursors between 180°C and 250°C. These conditions allowed the systematic formation of UO_{2+x}, nH_2O, even if HERFD-XANES analyses evidenced variations in the O/U ratio. Moreover, hydrothermal treatment at 250°C led to very low amounts of residual water and carbon, comparable to those obtained after thermal conversion of oxalates at 1000°C. Modifying the pH was also found to strongly affect the morphology of the final powders. Control on the final morphology was further enhanced by changing the precipitating agent used before hydrothermal treatment. Hydrothermal conversion of amorphous U(IV) aspartate led to precipitate monodisperse spherical particles, with an accurately size control in the 400 nm – 2.5 µm range. Once again, XRD analysis attested the formation of $UO_{2+x}.nH_2O$ samples, while TGA experiments revealed the presence of residual organics and water. Nevertheless, additional heat treatments performed up to 600°C led to produce anhydrous and carbon-free dense particles without altering their initial morphology. It also enabled to control the final stoichiometry of the particles from UO_{2+x} to U_3O_8 depending on the atmosphere used. Hydrothermal conversion of carboxylate precursors then appeared as an easy and efficient way to yield uranium oxide samples in solution. The absence of impurities as well as the possibility to monitor the samples morphology also allow the direct sintering of the powders prepared.

A preliminary study dedicated to sintering of the powders prepared was then undertaken and revealed their good densification ability. The sintering map of 3 different uranium oxides presenting different morphologies was established, and paves the way to the control of the final pellet's microstructure. The study of the densification revealed that after a 4-hours heat treatment at 1500°C, all the powders exhibited relative densities above 90%TD. In the case of single crystals and microspheres, densities greater than or equal to 96% were also obtained at 1700°C. In contrast, a sintering time of only 2 to 8 hours at 1500°C led to comparable results for nano-powders prepared at pH = 8, due to their higher reactivity. In order to complement numerical approaches, the elaboration of necks during the first step of UO_{2+x} microspheres sintering was also experimentally monitored by High Temperature Environmental Scanning Electron Microscopy (HT-ESEM). All our observations confirmed that the hydrothermal conversion of carboxylates is a promising route for the synthesis of actinide oxides, which can be subsequently sintered without any preliminary treatment. In terms of process, this allows the reduction of the number of steps by comparison to the thermal conversion conventionally carried out after oxalate precipitation.

This project has received funding from the EURATOM research and training programme 2017-2021 under grant agreement No 755171

LIST OF REFERENCES

1. Crawford, D. C.; Porter, D. L.; Hayes, S. L.: Fuels for sodium-cooled fast reactors: US perspective, *J Nucl Mater* **2007,** *371*, 202-231.
2. Vaudez, S.; Lechelle, J.; Berzati, S.; Heintz, J. M.: Assessing the oxygen stoichiometry during the sintering of (U, Pu)O_2 fuel, *J Nucl Mater* **2015,** *460*, 221-225.
3. Serp, J.; Poinssot, C.; Bourg, S.: Assessment of the Anticipated Environmental Footprint of Future Nuclear Energy Systems. Evidence of the Beneficial Effect of Extensive Recycling, *Energies* **2017,** *10*.
4. Vollath, D.; Wedemeyer, H.; Elbel, H.; Gunther, E.: On the Dissolution of (U,Pu)O_2 Solid-Solutions with Different Plutonium Contents in Boiling Nitric-Acid, *Nucl Technol* **1985,** *71*, 240-245.
5. Vaudez, S.; Belin, R. C.; Aufore, L.; Sornay, P.; Grandjean, S.: A new fabrication route for SFR fuel using (U, Pu)O_2 powder obtained by oxalic co-conversion, *J Nucl Mater* **2013,** *442*, 227-234.
6. Abraham, F.; Arab-Chapelet, B.; Rivenet, M.; Tamain, C.; Grandjean, S.: Actinide oxalates, solid state structures and applications, *Coord. Chem. Rev.* **2014,** *266-267*, 28-68.
7. Vigier, N.; Grandjean, S.; Arab-Chapelet, B.; Abraham, F.: Reaction mechanisms of the thermal conversion of Pu(IV) oxalate into plutonium oxide, *J Alloy Compd* **2007,** *444*, 594-597.
8. Desfougeres, L.; Welcomme, E.; Ollivier, M.; Martin, P. M.; Hennuyer, J.; Hunault, M. O. J. Y.; Podor, R.; Clavier, N.; Favergeon, L.: Oxidation as an Early Stage in the Multistep Thermal Decomposition of Uranium(IV) Oxalate into U_3O_8, *Inorg Chem* **2020,** *59*, 8589-8602.
9. Martinez, J.; Clavier, N.; Ducasse, T.; Mesbah, A.; Audubert, F.; Corso, B.; Vigier, N.; Dacheux, N.: From uranium(IV) oxalate to sintered UO_2: Consequences of the powders' thermal history on the microstructure, *J Eur Ceram Soc* **2015,** *35*, 4535-4546.
10. White, G. D.; Bray, L. A.; Hart, P. E.: Optimization of Thorium Oxalate Precipitation Conditions Relative to Derived Oxide Sinterability, *J Nucl Mater* **1981,** *96*, 305-313.
11. Asakura, K.; Takeuchi, K.: Effect of residual carbon on the sintering behavior of MOX pellets, *J Nucl Mater* **2006,** *348*, 165-173.
12. Chambon, C.; Vaudez, S.; Heintz, J. M.: De-densification mechanisms of yttria-doped cerium oxide during sintering in a reducing atmosphere, *J. Amer. Ceram. Soc.* **2018**.
13. Neck, V.; Kim, J. I.: Solubility and hydrolysis of tetravalent actinides, *Radiochim Acta* **2001,** *89*, 1-16.
14. Horlait, D.; Claparède, L.; Clavier, N.; Szenknect, S.; Dacheux, N.; Ravaux, J.; Podor, R.: Stability and Structural Evolution of $Ce^{IV}_{1-x}Ln^{III}_xO_{2-x/2}$ Solid Solutions: A Coupled μ-Raman/XRD Approach, *Inorg Chem* **2011,** *50*, 7150-7161.
15. Hubert, S.; Purans, J.; Heisbourg, G.; Moisy, P.; Dacheux, N.: Local structure of actinide dioxide solid solutions $Th_{1-x}U_xO_2$ and $Th_{1-x}Pu_xO_2$, *Inorg Chem* **2006,** *45*, 3887-3894.
16. Chen, P.-L.; Chen, I. W.: Grain Growth in CeO2: Dopant Effects, Defect Mechanism, and Solute Drag, *J Am Ceram Soc* **1996,** *79*, 1793-1800.
17. Gotte, A.; Spångberg, D.; Hermansson, K.; Baudin, M.: Molecular dynamics study of oxygen self-diffusion in reduced CeO_2, *Solid State Ionics* **2007,** *178*, 1421-1427.
18. Hingant, N.; Clavier, N.; Dacheux, N.; Hubert, S.; Barre, N.; Podor, R.; Aranda, L.: Preparation of morphology controlled $Th_{1-x}U_xO_2$ sintered pellets from low-temperature precursors, *Powder Technol* **2011,** *208*, 454-460.
19. Rabenau, A.: The Role of Hydrothermal Synthesis in Preparative Chemistry, *Angew Chem Int Edit* **1985,** *24*, 1026-1040.
20. Clavier, N.; Hingant, N.; Rivenet, M.; Obbade, S.; Dacheux, N.; Barre, N.; Abraham, F.: X-Ray Diffraction and μ-Raman Investigation of the Monoclinic-Orthorhombic Phase Transition in $Th_{1-x}U_x(C_2O_4)_2 \cdot 2H_2O$ Solid Solutions, *Inorg Chem* **2010,** *49*, 1921-1931.

This project has received funding from the EURATOM research and training programme 2017-2021 under grant agreement No 755171

21. Hutchings, M. T.: High-Temperature Studies of UO_2 and ThO_2 Using Neutron-Scattering Techniques, *J Chem Soc Farad T 2* **1987,** *83*, 1083-1103.
22. Bertrand, M.; Plasari, E.; Lebaigue, O.; Baron, P.; Lamarque, N.; Ducros, F.: Hybrid LES-multizonal modelling of the uranium oxalate precipitation, *Chem Eng Sci* **2012,** *77*, 95-104.
23. Abraham, F.; Arab-Chapelet, B.; Rivenet, M.; Tamain, C.; Grandjean, S.: Actinide oxalates, solid state structures and applications, *Coordin Chem Rev* **2014,** *266*, 28-68.
24. Crossey, L. J.: Thermal-Degradation of Aqueous Oxalate Species, *Geochim Cosmochim Ac* **1991,** *55*, 1515-1527.
25. Leinders, G.; Cardinaels, T.; Binnemans, K.; Verwerft, M.: Accurate lattice parameter measurements of stoichiometric uranium dioxide, *J Nucl Mater* **2015,** *459*, 135-142.
26. Blackburn, P. E.; Weissbart, J.; Gulbranson, E. A.: Oxidation of Uranium Dioxide, *J Phys Chem-Us* **1958,** *62*, 902-908.
27. Cardinaels, T.; Govers, K.; Vos, B.; Van den Berghe, S.; Verwerft, M.; de Tollenaere, L.; Maier, G.; Delafoy, C.: Chromia doped UO_2 fuel: Investigation of the lattice parameter, *J Nucl Mater* **2012,** *424*, 252-260.
28. Janeczek, J.; Ewing, R. C.: Structural Formula of Uraninite, *J Nucl Mater* **1992,** *190*, 128-132.
29. Janeczek, J.; Ewing, R. C.: X-Ray-Powder Diffraction Study of Annealed Uraninite, *J Nucl Mater* **1991,** *185*, 66-77.
30. Grønvold, F.: High-Temperature X-Ray Study of Uranium Oxides in the UO_2-U_3O_8 Region, *J Inorg Nucl Chem* **1955,** *1*, 357-370.
31. Desgranges, L.; Badinozzi, G.; Simeone, D.; Fischer, H. E.: Refinement of the a-U_4O_9 Crystalline Structure: New Insight into the U_4O_9 -> U_3O_8 Transformation, *Inorg Chem* **2011,** *50*, 6146-6151.
32. Hoekstra, H. R.; Santoro, A.; Siegel, S.: The Low Temperature Oxidation of UO_2 and U_4O_9, *J Inorg Nucl Chem* **1961,** *18*, 166-178.
33. Leinders, G.; Pakarinen, J.; Delville, R.; Cardinaels, T.; Binnemans, K.; Verwerft, M.: Low-Temperature Oxidation of Fine UO_2 Powders: A Process of Nanosized Domain Development, *Inorg Chem* **2016,** *55*, 3915-3927.
34. Cooper, R. I.; Willis, B. T. M.: Refinement of the structure of b-U_4O_9, *Acta Crystallographica a-Foundation and Advances* **2004,** *60*, 322-325.
35. Kvashnina, K. O.; Butorin, S. M.; Martin, P.; Glatzel, P.: Chemical State of Complex Uranium Oxides, *Phys Rev Lett* **2013,** *111*, 253002.
36. Gueneau, C.; Baichi, M.; Labroche, D.; Chatillon, C.; Sundman, B.: Thermodynamic assessment of the uranium-oxygen system, *J Nucl Mater* **2002,** *304*, 161-175.
37. Trillaud, V.; Maynadie, J.; Manaud, J.; Hidalgo, J.; Meyer, D.; Podor, R.; Dacheux, N.; Clavier, N.: Synthesis of size-controlled UO_2 microspheres from the hydrothermal conversion of U(IV) aspartate, *Crystengcomm* **2018,** *20*, 7749-7760.
38. Nkou Bouala, G. I.; Clavier, N.; Podor, R.; Cambedouzou, J.; Mesbah, A.; Brau, H. P.; Léchelle, J.; Dacheux, N.: Preparation and characterisation of uranium oxides with spherical shapes and hierarchical structures, *Crystengcomm* **2014,** *16*, 6944-6954.
39. Balakrishna, P.; Varma, B. P.; Krishnan, T. S.; Mohan, T. R. R.; Ramakrishnan, P.: Thorium Oxide - Calcination, Compaction and Sintering, *J Nucl Mater* **1988,** *160*, 88-94.
40. Balice, L.; Bouexiere, D.; Cologna, M.; Cambriani, A.; Vigier, J. F.; De Bona, E.; Soraru, G. D.; Kubel, C.; Walter, O.; Popa, K.: Nano and micro $U_{1-x}Th_xO_2$ solid solutions: From powders to pellets, *J Nucl Mater* **2018,** *498*, 307-313.
41. Popa, K.; Walter, O.; Blanco, O. D.; Guiot, A.; Bouexiere, D.; Colle, J. Y.; Martel, L.; Naji, M.; Manara, D.: A low-temperature synthesis method for AnO_2 nanocrystals (An = Th, U, Np, and Pu) and associate solid solutions, *Crystengcomm* **2018,** *20*, 4614-4622.
42. Walter, O.; Popa, K.; Blanco, O. D.: Hydrothermal decomposition of actinide(IV) oxalates: a new aqueous route towards reactive actinide oxide nanocrystals, *Open Chem* **2016,** *14*, 170-174.

43. Martinez, J.; Clavier, N.; Mesbah, A.; Audubert, F.; Le Goff, X. F.; Vigier, N.; Dacheux, N.: An original precipitation route toward the preparation and the sintering of highly reactive uranium cerium dioxide powders, *J Nucl Mater* **2015,** *462*, 173-181.
44. Plasil, J.: The crystal structure of uranyl-oxide mineral schoepite, [(UO2)(4)O(OH)(6)](H2O)(6), revisited, *J Geosci-Czech* **2018,** *63*, 65-73.
45. Nakashima, S.: Kinetics and Thermodynamics of U-Reduction by Natural and Simple Organic-Matter, *Org Geochem* **1992,** *19*, 421-430.
46. Nakashima, S.: Complexation and Reduction of Uranium by Lignite, *Sci Total Environ* **1992,** *118*, 425-437.
47. Mudher, K. D. S.; Krishnan, K.; Chadha, A. K.; Venugopal, V.: Thermal and X-ray studies on mixed metal oxalates - $(NH_4)Ln(III)U(IV)(C_2O_4)_4$. $8H_2O$ (Ln = La, Ce, Pr, Nd Tb), *Thermochim Acta* **1997,** *297*, 169-175.
48. Andres, Y.; MacCordick, H. J.; Hubert, J. C.: Selective biosorption of thorium ions by an immobilized mycobacterial biomass, *Appl Microbiol Biot* **1995,** *44*, 271-276.
49. Humelnicu, D.; Drochioiu, G.; Popa, K.: Bioaccumulation of thorium and uranyl ions on Saccharomyces cerevisiae, *J Radioanal Nucl Chem* **2004,** *260*, 291-293.
50. Sato, N.; Quitain, A. T.; Kang, K.; Daimon, H.; Fujie, K.: Reaction kinetics of amino acid decomposition in high-temperature and high-pressure water, *Ind Eng Chem Res* **2004,** *43*, 3217-3222.
51. Dacheux, N.; Aupiais, J.: Determination of uranium, thorium, plutonium, americium, and curium ultratraces by photon electron rejecting alpha liquid scintillation, *Anal Chem* **1997,** *69*, 2275-2282.
52. Lamarque, N.; Zoppe, B.; Lebaigue, O.; Dolias, Y.; Bertrand, M.; Ducros, F.: Large-eddy simulation of the turbulent free-surface flow in an unbaffled stirred tank reactor, *Chem Eng Sci* **2010,** *65*, 4307-4322.
53. Walter, O.; Popa, K.; Dieste Blanco, O.: Hydrothermal decomposition of actinide(IV) oxalates: a new aqueous route towards reactive actinide oxide nanocrystals, *Open Chem* **2016,** *14*, 170-174.
54. Rai, D.; Felmy, A. R.; Ryan, J. L.: Uranium(IV) Hydrolysis Constants and Solubility Product of $UO_2.xH_2O$(am), *Inorg Chem* **1990,** *29*, 260-264.
55. Clavier, N.; Maynadie, J.; Mesbah, A.; Hidalgo, J.; Lauwerier, R.; Bouala, G. I. N.; Parres-Maynadie, S.; Meyer, D.; Dacheux, N.; Podor, R.: Thorium aspartate tetrahydrate precursor to ThO_2: Comparison of hydrothermal and thermal conversions, *J Nucl Mater* **2017,** *487*, 331-342.
56. Faisal, M.; Sato, N.; Quitain, A. T.; Daimon, H.; Fujie, K.: Reaction kinetics and pathway of hydrothermal decomposition of aspartic acid, *Int J Chem Kinet* **2007,** *39*, 175-180.
57. Deguchi, S.; Ghosh, S. K.; Alargova, R. G.; Tsujii, K.: Viscosity measurements of water at high temperatures and pressures using dynamic light scattering, *J Phys Chem B* **2006,** *110*, 18358-18362.
58. Sung, M. H.; Choi, I. S.; Kim, J. S.; Kim, W. S.: Agglomeration of yttrium oxalate particles produced by reaction precipitation in semi-batch reactor, *Chem Eng Sci* **2000,** *55*, 2173-2184.
59. Li, W.; Gao, L.: Rapid sintering of nanocrystalline ZrO_2(3Y) by spark plasma sintering, *J Eur Ceram Soc* **2000,** *20*, 2441-2445.
60. Hallberg, H.; Zhu, Y. C.: Stability of grain boundary texture during isothermal grain growth in UO2 considering anisotropic grain boundary properties, *J Nucl Mater* **2015,** *465*, 664-673.
61. Kang, S. J. L.; Jung, Y. I.: Sintering kinetics at final stage sintering: model calculation and map construction, *Acta Mater* **2004,** *52*, 4573-4578.
62. Kanters, J.; Eisele, U.; Rodel, J.: Effect of initial grain size on sintering trajectories, *Acta Mater* **2000,** *48*, 1239-1246.
63. Clavier, N.; Podor, R.; Deliere, L.; Ravaux, J.; Dacheux, N.: Combining *in situ* HT-ESEM observations and dilatometry: An original and fast way to the sintering map of ThO_2, *Mater Chem Phys* **2013,** *137*, 742-749.

This project has received funding from the EURATOM research and training programme 2017-2021 under grant agreement No 755171

64. Cherkaski, Y.; Clavier, N.; Brissonneau, L.; Podor, R.; Dacheux, N.: Densification behavior and microstructure evolution of yttrium-doped ThO_2 ceramics, *J Eur Ceram Soc* **2017,** *37*, 3381-3391.
65. Simeon, J.; Lebreton, F.; Ramond, L.; La Lumia, F.; Clavier, N.; Bernard-Granger, G.: Sintering of a UO_2-PuO_2 freeze-granulated powder under reducing conditions, *J Eur Ceram Soc* **2020,** *40*, 5900-5908.
66. Qin, D.; Mesbah, A.; Lautru, J.; Szenknect, S.; Dacheux, N.; Clavier, N.: Reaction sintering of rhabdophane into monazite-cheralite $Nd_{1-2x}Th_xCa_xPO_4$ (x = 0 – 0.1) ceramics, *J Eur Ceram Soc* **2020,** *40*, 911-922.
67. Clausell, C.; Barba, A.; Nuno, L.; Jarque, J. C.: Effect of average grain size and sintered relative density on the imaginary part - mu" of the complex magnetic permeability of $(Cu_{0.12}Ni_{0.23}Zn_{0.65})Fe_2O_4$ system, *Ceram Int* **2016,** *42*, 4256-4261.
68. Bernard-Granger, G.; Guizard, C.; Addad, A.: Sintering of an ultra pure alpha-alumina powder: I. Densification, grain growth and sintering path, *J Mater Sci* **2007,** *42*, 6316-6324.
69. Chretien, L.; Bonnet, L.; Boulesteix, R.; Maitre, A.; Salle, C.; Brenier, A.: Influence of hot isostatic pressing on sintering trajectory and optical properties of transparent Nd:YAG ceramics, *J Eur Ceram Soc* **2016,** *36*, 2035-2042.
70. Bernache-Assollant, D., *Chimie-Physique du Frittage*. Paris, 1993.
71. Tyrpekl, V.; Cologna, M.; Robba, D.; Somers, J.: Sintering behaviour of nanocrystalline ThO_2 powder using spark plasma sintering, *J Eur Ceram Soc* **2016,** *36*, 767-772.
72. Cologna, M.; Tyrpekl, V.; Ernstberger, M.; Stohr, S.; Somers, J.: Sub-micrometre grained UO_2 pellets consolidated from sol gel beads using spark plasma sintering (SPS), *Ceram Int* **2016,** *42*, 6619-6623.
73. Zhang, T. S.; Hing, P.; Huang, H. T.; Kilner, J.: Sintering and grain growth of CoO-doped CeO_2 ceramics, *J Eur Ceram Soc* **2002,** *22*, 27-34.
74. Mullins, W. W.; Vinals, J.: Scaling in Linear Bubble Models of Grain-Growth, *Acta Metall Mater* **1993,** *41*, 1359-1367.
75. Podor, R.; Clavier, N.; Ravaux, J.; Claparede, L.; Dacheux, N.: *In Situ* HT-ESEM Observation of CeO_2 Grain Growth During Sintering, *J Am Ceram Soc* **2012,** *95*, 3683-3690.
76. Maitre, A.; Beyssen, D.; Podor, R.: Modelling of the grain growth and the densification of SnO_2-based ceramics, *Ceram Int* **2008,** *34*, 27-35.
77. Srolovitz, D. J.; Anderson, M. P.; Grest, G. S.; Sahni, P. S.: Computer-Simulation of Grain-Growth .3. Influence of a Particle Dispersion, *Acta Metallurgica* **1984,** *32*, 1429-1438.
78. Manaud, J.; Maynadie, J.; Mesbah, A.; Hunault, M. O. J. Y.; Martin, P.; Zunino, M.; Dacheux, N.; Clavier, N.: Hydrothermal Conversion of Thorium Oxalate into into $ThO_2{\cdot}nH_2O$ oxide, *Inorg Chem* **2020,** *59*, 14954-14966.
79. Nkou Bouala, G. I.; Clavier, N.; Lechelle, J.; Monnier, J.; Ricolleau, C.; Dacheux, N.; Podor, R.: High-temperature electron microscopy study of ThO_2 microspheres sintering, *J Eur Ceram Soc* **2017,** *37*, 727-738.
80. Bannister, M. J.; Buykx, W. J.: Sintering Mechanism in UO_{2+x}, *J Nucl Mater* **1977,** *64*, 57-65.
81. Halldahl, L.: Quasi-Isothermal Dilatometric Sintering Studies on UO_2 Powder Compacts - Method of Evaluation and Influence of Experimental Parameters, *Thermochim Acta* **1982,** *58*, 261-270.
82. Bacmann, J. J.; Cizeron, G.: Mechanisms in Incipient Uranium Dioxide Calcination, *J Nucl Mater* **1969,** *33*, 271-285.
83. Dehaudt, P.; Bourgeois, L.; Chevrel, H.: Activation energy of UO_2 and UO_{2+x} sintering, *J Nucl Mater* **2001,** *299*, 250-259.
84. Scott, R.; Hall, A. R.; Williams, J.: The Plastic Deformation of Uranium Oxides above 800°C, *J Nucl Mater* **1959,** *1*, 39-48.
85. Amato, I.; Colombo, R. L.; Protti, A. M.: On the Activation Energy of Sintering Non-Stoichiometric Uranium Oxide, *J Nucl Mater* **1964,** *11*, 229-235.

This project has received funding from the EURATOM research and training programme 2017-2021 under grant agreement No 755171

86. Lay, K. W.: Initial Sintering Kinetics of Hyperstoichiometric Uranium Dioxide, *J Am Ceram Soc* **1971,** *54*, 18-&.
87. Shukla, S.; Seal, S.; Vij, R.; Bandyopadhyay, S.: Reduced activation energy for grain growth in nanocrystalline yttria-stabilized zirconia, *Nano Lett* **2003,** *3*, 397-401.
88. Wang, C. J.; Huang, W. Z.; Wang, Y.; Cheng, Y. L.; Zou, B. L.; Fan, X. Z.; Yang, J. L.; Cao, X. Q.: Synthesis of monodispersed $La_2Ce_2O_7$ nanocrystals via hydrothermal method: A study of crystal growth and sintering behavior, *Int J Refract Met H* **2012,** *31*, 242-246.
89. Mohan, A.; Soni, N. C.; Moorthy, V. K.: Sintering Diagrams of UO_2, *J Nucl Mater* **1979,** *79*, 312-322.
90. Lahiri, D.; Rao, S. V. R.; Rao, G. V. S. H.; Srivastava, R. K.: Study on sintering kinetics and activation energy of UO_2 pellets using three different methods, *J Nucl Mater* **2006,** *357*, 88-96.
91. Wakai, F.: Modeling and simulation of elementary processes in ideal sintering, *J Am Ceram Soc* **2006,** *89*, 1471-1484.
92. Bordere, S.; Bernard, D.: Full resolution of the Monte Carlo time scale demonstrated through the modelling of two-amorphous-particles sintering, *Comp Mater Sci* **2008,** *43*, 1074-1080.
93. Martin, S.; Parekh, R.; Guessasma, M.; Lechelle, J.; Fortin, J.; Saleh, K.: Study of the sintering kinetics of bimodal powders. A parametric DEM study, *Powder Technol* **2015,** *270*, 637-645.
94. El-Sayed Ali, M.; Lorenzelli, R.: Kinetics of Initial-Stage of Sintering of UO_2 and UO_2 with Nd_2O_3 Addition, *J Nucl Mater* **1979,** *87*, 90-96.
95. Woolfrey, J. L.: Effect of Green Density on Initial-Stage Sintering Kinetics of UO_2, *J Am Ceram Soc* **1972,** *55*, 383-389.
96. Burton, B.; Reynolds, G. L.: Influence of Deviations from Stoichiometric Composition on Diffusional Creep of Uranium-Dioxide, *Acta Metallurgica* **1973,** *21*, 1641-1647.
97. Kutty, T. R. G.; Hegde, P. V.; Khan, K. B.; Basak, U.; Pillai, S. N.; Sengupta, A. K.; Jain, G. C.; Majumdar, S.; Kamath, H. S.; Purushotham, D. S. C.: Densification behaviour of UO_2 in six different atmospheres, *J Nucl Mater* **2002,** *305*, 159-168.
98. Knorr, D. B.; Cannon, R. M.; Coble, R. L.: An Analysis of Diffusion and Diffusional Creep in Stoichiometric and Hyperstoichiometric Uranium-Dioxide, *Acta Metallurgica* **1989,** *37*, 2103-2123.
99. Nkou Bouala, G. I.; Clavier, N.; Martin, S.; Lechelle, J.; Favrichon, J.; Brau, H. P.; Dacheux, N.; Podor, R.: From in Situ HT-ESEM Observations to Simulation: How Does Polycrystallinity Affects the Sintering of CeO_2 Microspheres?, *J Phys Chem C* **2016,** *120*, 386-395.
100. Utlak, S. A.; McMurray, J. W.: Thermodynamic modeling of the U_3O_{8-x} solid solution phase, *J Nucl Mater* **2020,** *530*.
101. Quemard, L.; Desgranges, L.; Bouineau, V.; Pijolat, M.; Baldinozzi, G.; Millot, N.; Niepce, J. C.; Poulesquen, A.: On the origin of the sigmoid shape in the UO_2 oxidation weight gain curves, *J Eur Ceram Soc* **2009,** *29*, 2791-2798.
102. Kuczynski, G. C.: The Mechanism of Densification during Sintering of Metallic Particles, *Acta Metallurgica* **1956,** *4*, 58-61.
103. Ristic, M. M.; Kostic, E.: Etude du procédé de frittage du dioxyde d'uranium d'après la théorie de Pines, *Nuclear Science Abstracts* **1964,** *18*, NP-14124.
104. Lay, K. W.; Carter, R. E.: Role of O/U Ratio on Sintering of UO_2, *J Nucl Mater* **1969,** *30*, 74-87.
105. Ainscough, J. B.; Oldfield, B. W.; Ware, J. O.: Isothermal Grain-Growth Kinetics in Sintered UO_2 Pellets, *J Nucl Mater* **1973,** *49*, 117-128.
106. Singh, R. N.: Isothermal Grain-Growth Kinetics in Sintered UO_2 Pellets, *J Nucl Mater* **1977,** *64*, 174-178.
107. Yang, J. H.; Kang, K. W.; Kim, K. S.; Rhee, Y. W.; Song, K. W.: Recycling Process for Sinter-Active U_3O_8 Powders, *J Nucl Sci Technol* **2010,** *47*, 538-541.
108. Song, K. W.; Kim, K. S.; Kim, Y. M.; Jung, Y. H.: Sintering of mixed UO_2 and U_3O_8 powder compacts, *J Nucl Mater* **2000,** *277*, 123-129.

This project has received funding from the EURATOM research and training programme 2017-2021 under grant agreement No 755171

109. Herring, C.: Effect of Change of Scale on Sintering Phenomena, *J Appl Phys* **1950,** *21*, 301-303.
110. Lequitte, M.; Autissier, D.: Synthesis and sintering of nanocrystalline erbium oxide, *Nanostruct Mater* **1995,** *6*, 333-336.
111. Lechelle, J.; Boyer, R.; Trotabas, M.: A mechanistic approach of the sintering of nuclear fuel ceramics, *Mater Chem Phys* **2001,** *67*, 120-132.

This project has received funding from the EURATOM research and training programme 2017-2021 under grant agreement No 755171